Design and Analysis of Cooling Methods for Solar Panels

by

Adam M. Palumbo

Submitted in Partial Fulfillment of the Requirements

for the Degree of

Master of Science in Engineering

in the

Mechanical Engineering

Program

YOUNGSTOWN STATE UNIVERSITY

December, 2013

Design and Analysis of Cooling Methods for Solar Panels

Adam M. Palumbo

I hereby release this thesis to the public. I understand that this thesis will be made available from the OhioLINK ETD Center and the Maag Library Circulation Desk for public access. I also authorize the University or other individuals to make copies of this thesis as needed for scholarly research.

Signature:

Adam M. Palumbo, Student Date

Approvals:

Dr. Ganesh Kudav, Thesis Advisor Date

Dr. Hazel Marie, Committee Member Date

Dr. Douglas M. Price, Committee Member Date

Dr. Salvatore A. Sanders, Associate Dean, Graduate Studies Date

Abstract

As the future progresses, many companies and industries are striving to achieve a "greener" approach to energy production by using solar energy. Solar panels that use PV cells (semiconductor devices used to convert light into electrical energy) are popular for converting solar power into electricity. One of the problems in using PV cells to extract energy from sunlight is the temperature effect on PV cells. As the solar panel is heated, the conversion efficiency of light to electrical energy is diminished. Because solar panels can be expensive, it is important to be able to extract as much energy as possible. This thesis proposes cooling methods for the panel in order to achieve optimum efficiency. To achieve this, various cooling methods have been proposed. A bare solar panel with no air velocity was used as a base model. This was tested and compared to bare solar panels cooled by heat sinks, in the form of extended surfaces such as plate fins, that can be mounted on the back surface of solar panels. These heat sinks were also tested for still air and different air velocities. Analytical calculations were also performed for the case of a bare panel with natural convection. Finally, computational models were made in ANSYS to obtain results that were compared with the experimental and analytical results. Other methods are discussed including using a pump to cool the panels using water or a coolant.

Results showed that the heat sinks were only marginally effective; they resulted in a steady-state temperature of only a few degrees less than a solar panel without a heat sink. Due to these results, it is proposed that pump cooling would be far more beneficial. With the correctly sized pump, the temperature can be made to closely match any desired value. The results are presented in the following thesis.

Acknowledgements

Thesis Advisor

Dr. Ganesh Kudav

Thesis Committee

Dr. Price, Dr. Marie

Corporate Partners

Q4 Manufacturing Solutions, Youngstown, OH

Faculty

Dr. Ganesh Kudav, Dr. Hazel Marie, Dr. Hyun W. Kim, Dr. Darrel Wallace, Dr. Daniel Suchora

Additional Assistance

Richard Laughlin, YSU Electrical Maintenance Dept.

Maureen Adams, Department of Mechanical & Industrial Engineering Secretary

Bob Schmitt and John Dodson, YSU Machine Shop

Students

Mike Kovach, Nick Matune, John Terzak

Dedication

First and foremost, I would like to dedicate this thesis to my Grandma Mullett for working to instill knowledge in me starting at an extremely young age. You helped pique my curiosity and educate my mind when it was at its most fertile state for expansion. I have you to thank for all my academic achievements.

I would like to thank Dr. Kudav and the rest of the Mechanical Engineering Program for giving me the great opportunity to work on a thesis project during my graduate studies at Youngstown State University. The amount of knowledge and experience I have gained during my thesis has been immeasurable.

During the last two years, there have been countless people who have helped me with my project every step of the way. I would like to thank Dr. Kudav, Dr. Marie, Dr. Kim, Dr. Wallace, and Richard Laughlin from Electrical Maintenance for the equipment loaned and advice given on countless occasions. Maureen Adams was also a huge help in the various orders she placed for equipment I needed. I would also like to extend my gratitude towards my friends and classmates, Mike Kovach, Nick Matune, and John Terzak, as well as Bob Schmitt and John Dodson from the machine shop, for the many hours spent assisting me in assembling my experimental setup.

I would also like to thank Dr. Suchora for the never-ending wisdom he has imparted on me during my college experience.

Lastly, I would like to thank Youngstown State University and the Cushwa family for presenting me with the amazing opportunities I have received through the Cushwa

Fellowship position. Without all of you, none of this would have been possible. Thank you all!!

Contents

List of Figures

Page

List of Tables

Page

Nomenclature

α	Thermal diffusivity
$\bar{h}$	Average convection heat transfer coefficient
$\bar{Nu}_s$	Nusselt number for finned surface
β	Coefficient of volume expansion
β_{sol}	Solar altitude
ΔT_e	Exit temperature difference, $T_s - T_e$
ΔT_i	Inlet temperature difference, $T_s - T_i$
ΔT_{lm}	Log mean temperature difference
δ	Declination angle of sun
$\dot{m}$	Mass flow rate
$\dot{Q}$	Heat transfer rate
$\dot{q}_o$	Heat flux into panel - irradiance
ϵ	Emmisivity
η	Panel efficiency
ν	Kinematic viscosity

σ	Stefan-Boltzmann constant, = 5.67 x $10^{-8} \frac{W}{m^2 \cdot K^4}$
A	Apparant solar irradiation at air mass equal to zero
A_s	Surface area
B	Atmospheric extinction coefficient
C	Ratio of diffuse irradiation on a horizontal surface to direct normal irradiation
c_p	Specific heat capacity
G_d	Direct radiation
G_R	Reflected radiation incident on surface
G_t	Total irradiance on surface
G_{ND}	Normal direction irradiation
h	Hour angle
h_1	Convection heat transfer coefficient at top surface
h_2	Convection heat transfer coefficient at bottom surface
h_{rad}	Radiation heat transfer coefficient
h_x	Local convection heat transfer coefficient
k_{eq}	Equivalent thermal conductivity for multiple layers
L	Thickness of solar panel
l	Latitiude
L_c	Characteristic length
L_{fin}	Length of channel

L_{panel} Length of panel

n Combination parameter for Nusselt number

NTU Number of transfer units

Nu_b Nusselt number for flow between plates

Nu_x Local Nusselt number

p Perimeter

P_{ss} Power at steady-state

Pr Prandtl number

R Thermal resistance

Ra_L Rayleigh number

Ra_s Rayleigh number for finned surface

Re_b^* Reynolds number for channel flow

Re_L Reynolds number

S_{fin} Spacing between fins

T Temperature

t Time

$T(0)$ Temperature at top surface of panel

$T(L)$ Temperature at bottom surface of panel

$T_{\infty 1}$ Ambient air temperature at top of panel

$T_{\infty 2}$ Ambient air temperature at bottom of panel

T_e Exit temperature

T_{film} Film temperature

T_i Inlet temperature

T_{ss} Steady-state temperature

T_{surr} Temperature of sourroundings

T_s Temperature of radiating surface

V Velocity of air

Chapter 1

Introduction to Solar Energy

Renewable energy has become a large focus for many scientists and engineers in recent years, due to the growing concern of environmental pollutants given off by the burning of non-renewable fossil fuels. The use of solar energy is seen as one of the cleanest and most widely available alternatives to current sources of energy. There are many options available for collecting solar power. This is due to two sources of solar energy; thermal and photovoltaic [Shahsavar et al., 2011].

Solar energy is obtained by collecting the energy that the sun gives off as radiation. In general, thermal systems rely on the energy created by the radiation to heat up a fluid. Photovoltaics, on the other hand, use the light given off by the sun to convert to electricity. There also exists a special method of collecting thermal energy known as Concentrating Solar Power (CSP), which involves using an optical device to concentrate the incoming radiation to a smaller area on a collector in order to minimize heat losses [Duffie and Beckman, 2006]. The higher temperatures created through CSP can be used to boil water and create steam. This in turn drives a turbine which converts the power into electricity. Examples of solar thermal power, photovoltaics, and CSP are shown in Figures 1.1, 1.2, and 1.3, respectively.

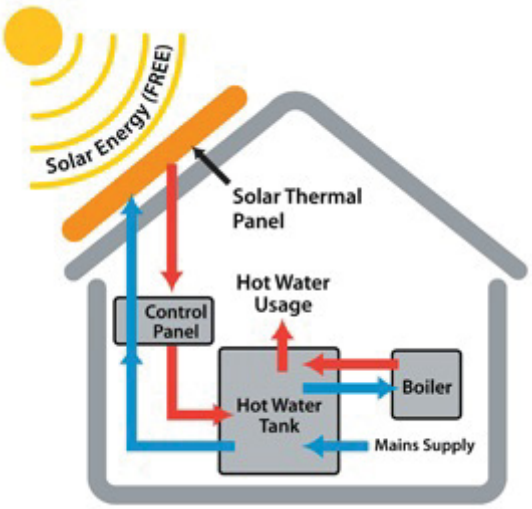

Figure 1.1: Schematic Showing Solar Thermal Power [Solar Thermal Energy]

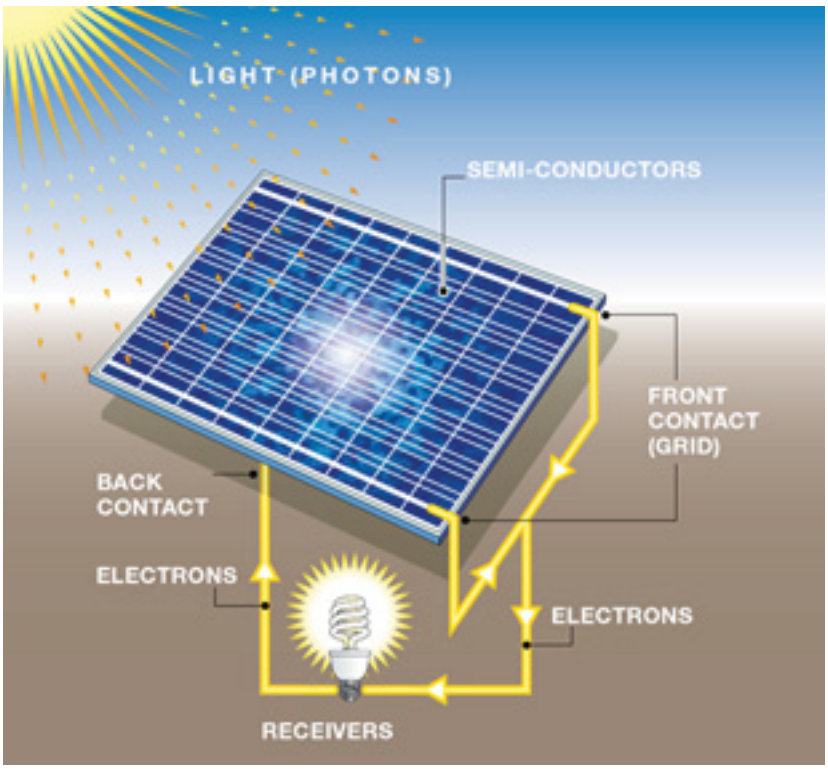

Figure 1.2: Schematic Showing Photovoltaic Power Source [How Photovoltaic Solar Cells Work]

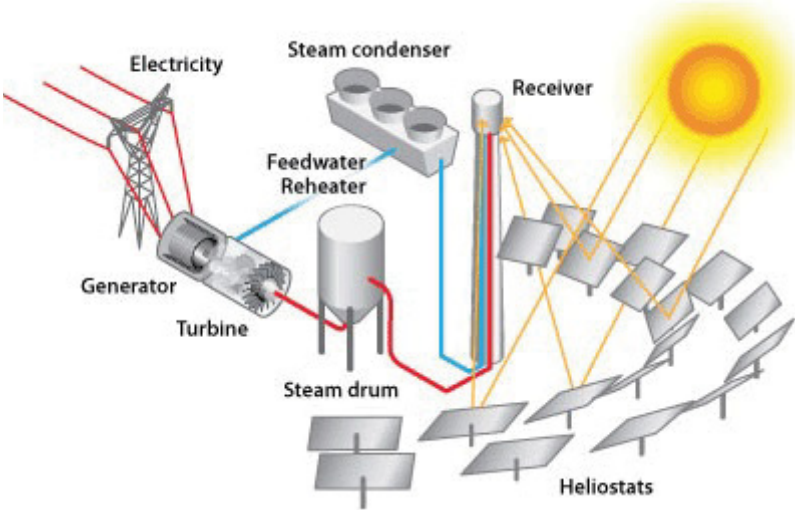

Figure 1.3: Schematic Showing Concentrating Solar Power (CSP) [A Power Tower Power Plant]

Solar engineers have faced multiple problems for each method. For instance, there can be heat losses in thermal systems and only a percentage of potential light is actually converted to electricity in photovoltaics. Solar power can also be expensive in many ways. While the energy source itself is free, the systems used to collect and store this energy may not be economically feasible in some cases. For this reason, it is crucial for solar engineers to discover new and innovative ways to increase the efficiency of solar units while simultaneously redesigning them in order to reduce the manufacturing and maintenance costs.

There are two main methods of utilizing the sun's energy: passive and active [Ogueke et al., 2009]. The passive method harnesses solar energy without the use of mechanical device. This can be as simple as placing large windows in a house to let sunlight in. The active method, however, uses mechanical systems such as solar panels and solar collectors. This thesis focuses primarily on active methods; more specifically, through the use of photovoltaics.

Many large scale solar energy systems exist in the United States. Currently, the photovoltaic system with the largest output is called the Agua Caliente Solar Project, created by NRG Energy. Array of solar panels is mounted on the ground and consist

of 5,200,000 modules manufactured by First Solar. Upon completion in 2014, the entire system is expected to generate 290MW of power. This is enough to provide power for approximately 100,000 homes [Agua Caliente Solar Project]. Figure 1.4 illustrates how large-scale the project is.

Figure 1.4: Agua Caliente Solar Project

Chapter 2

Photovoltaic Cells

2.1 General Information

Photovoltaic (PV) solar cells are typically made of crystalline silicon (Si). Circular PV cells are embedded into a plastic sheet in order to make a panel. It is known that the performance of PV cells is affected by irradiance, module temperature, and solar spectrum distribution [Fukishige, 2009]. This is due to the energy being converted from light energy in the photons to electrical energy. At the molecular level, the electrons become excited due to a high amount of thermal energy. This ends up dominating the electrical properties of the semi-conductor used in the solar panel. The temperature affects the voltage and current in the PV generator. While atmospheric temperature tends to have a small effect on the cell's operating temperature, the solar irradiance and wind speed both have a large effect [Skoplaki et al., 2008].

2.2 Temperature Effect

PV cells are affected by temperature in a negative way due to the negative temperature coefficient of crystalline silicon. This temperature coefficient is estimated to be in the range of -0.4 to -0.5%/K [Lee et al., 2008]. This causes the efficiency of the cells

(which are typically around 12% using a reference temperature of 25℃) to decrease. It has been shown that a decrease in the temperature of the solar panel can cause a 2% increase in the efficiency of the PV cells, when the carrier fluid (such as water) has a mass flow rate of 0.01 kg/s [Joshi and Tiwari, 2007]. An increase in efficiency is vital to the development of solar panels, as it would save money while providing greater amounts of energy. PV cells have the potential to be extremely efficient. Even in the worst-case scenario, a PV cell has an efficiency limit of 28.9% [Tayebjee et al., 2010]. Figure 2.1 shows the linear relationship of efficiency versus the module temperature. As can be seen, the conversion efficiency drops as the module temperature increases.

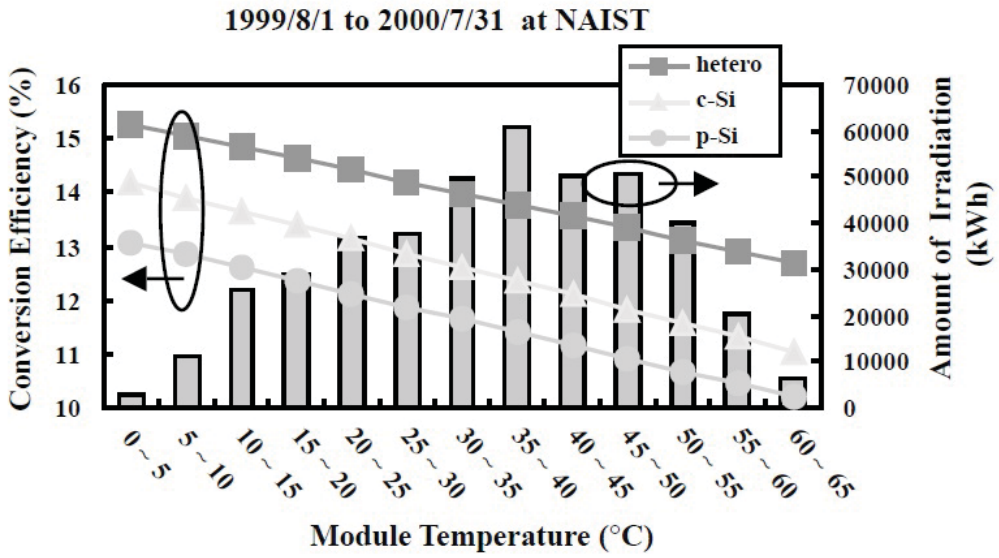

Figure 2.1: Variation of Efficiency as a Function of Module Temperature [Nishioka et al., 2011]

Since the radiation absorbed by the solar panel is converted to thermal energy as well as electrical energy, it is important to perform an energy balance on the system to see how efficient the solar panel will be at different operating temperatures. This allows the designer to project how much electrical power will be generated, so the design can be refined in order to generate the proper amount for the solar panel's required load. The maximum power as a function of cell temperature can be graphed at different radiation levels, as shown in Figure 2.2.

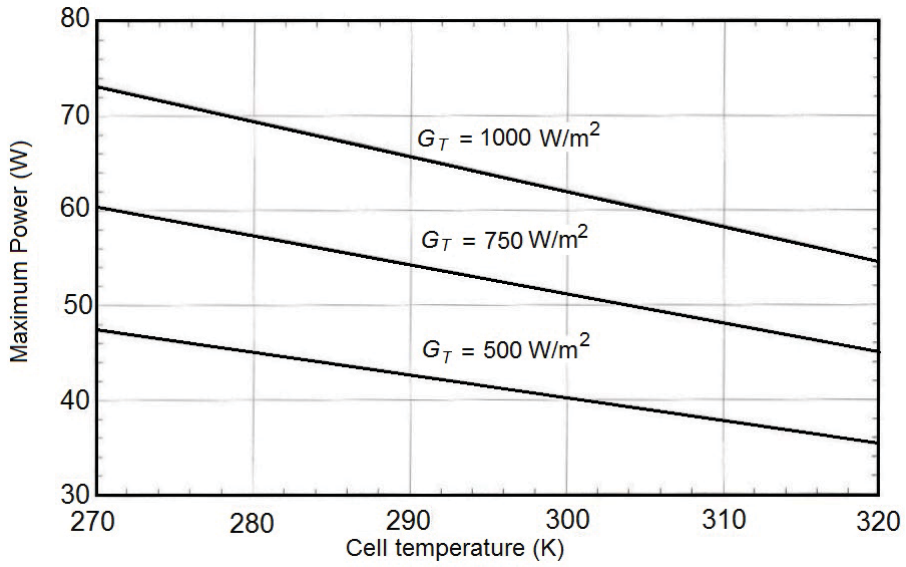

Figure 2.2: Variation of Power as a Function of Cell Temperature [Duffie and Beckman, 2006]

2.3 Increasing Efficiency

In recent years, there have been many attempts to curb the decrease in efficiency. One such method is using a hybrid photovoltaic-thermal cell (PV/T) [Lee et al., 2008]. This method is shown to be effective for overall efficiency; however, the efficiency of the PV cells is still diminished. Jet impingement cooling devices have also been used to lower the temperature of solar panels. In this method, small pipes run through the plate that the PV cells are mounted on. Water runs through the pipes and the heat is transferred to the water. The water drains out constantly as new water is pumped in [Royne and Dey, 2007]. Another method adds textures to the outer layer of the solar panel. These textures allow the light to be trapped more effectively. Using a specific surface texture which creates a v-shaped geometry allows the efficiency to increase as much as 52% for a 170 nm thick solar cell [Rim et al., 2007].

Similarly to adjusting the surface texture would be to create finned surfaces on the underside of the solar panel in order to increase the convection rate from which the heat leaves the back of the solar panel. The purpose of this thesis was to investigate how

different configurations of fins will affect the surface temperature and ultimately the efficiency of the PV cells. Various computer models were created in which numerous fin geometries were analyzed in order to find an optimal design to keep the surface temperature of the solar panel as close as possible to the ambient temperature.

2.4 Current-Voltage Characteristic of PV Cells

To understand the performance of photovoltaic cells, it is important to find the current-voltage characteristic, otherwise known as an I-V curve. The current-voltage characteristic is a graphical representation of the solar cell's output current as a function of voltage. This characterization is achieved by approximating the solar cell (or module) with an equivalent circuit consisting of a current source in parallel with a single diode, as shown in Figure 2.3 [Ishibashi et al., 2008]. Using a diode to model the cells gives a nonlinear current-voltage characteristic, which does not obey Ohm's Law. With zero irradiance, the solar cell will behave like a diode without a current source ["Part II - Photovoltaic Cell I-V Characterization Theory and LabVIEW Analysis Code"]. This will give an I-V curve that begins at a value of 0 amps. As the voltage increases, the current drops into the fourth quadrant of an xy graph, in the complex plane (real voltage value, imaginary current value). As light intensity is increased, the values needed to characterize the system are in the first quadrant.

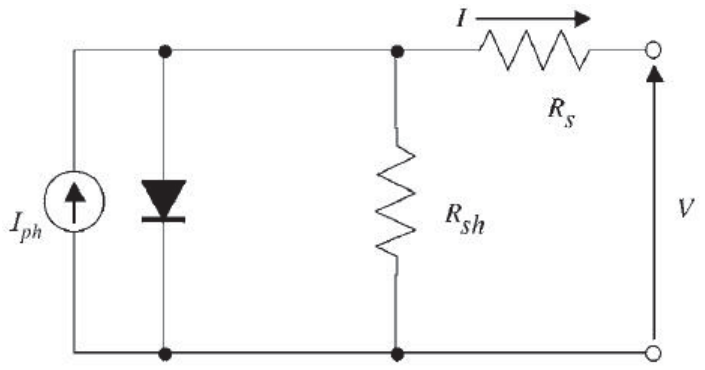

Figure 2.3: Equivalent Circuit of a Solar Cell [Ishibashi et al., 2012]

When the I-V curve is shown on a graph (as in Figure 2.4), it can be seen that the short circuit current (I_{sc}) can be read where the curve intersects the y-axis (voltage equals zero). Similarly, the open circuit voltage (V_{oc}) is shown where the I-V curve intersects the x-axis (where the current equals zero). Using Joule's law, the voltage can be multiplied by the corresponding current at that point in order to find the power generated by the solar cell. The power can be calculated along the entire curve in order to find the maximum power. The voltage at this point is known as V_{mpp}, and the current known as I_{mpp} [Duffie and Beckman, 2006]. This is the most important point in the current-voltage characteristic, as it is used to find the efficiency of the solar cell. The curve can be seen to decrease with a small slope. Upon reaching maximum power, the power decrease is achieved faster as the negative slope increases to a larger number before reaching the open circuit voltage.

The maximum power is often compared to the power found from the product of open circuit voltage and short circuit current (known as the theoretical power). The ratio between the two, respectively, is called the fill factor (ff) [Desilvestro, 2008]. Ideally, the fill factor would be as close to 1 as possible in order to take advantage of the full potential of the solar cells. However, the fill factor in practice will always be less than unity. Once the fill factor is known for each level of irradiation, the maximum power can be calculated by multiplying the fill factor by the theoretical power [Desilvestro, 2008]. The power voltage curve (P-V curve) is often shown on the same graph as the I-V curve. This shows the power generated by the solar cell as a function of voltage, with the power on a secondary y-axis. The peak of this curve shows the maximum power generated. The P-V curve will cross through the origin at a power of zero. After the peak at maximum power, the curve will decrease before crossing the x-axis at the open circuit voltage. A graph showing the I-V curve, P-V curve, fill factor, open circuit voltage, short circuit current, and maximum power generated is shown in Figure 2.4 [Desilvestro, 2008].

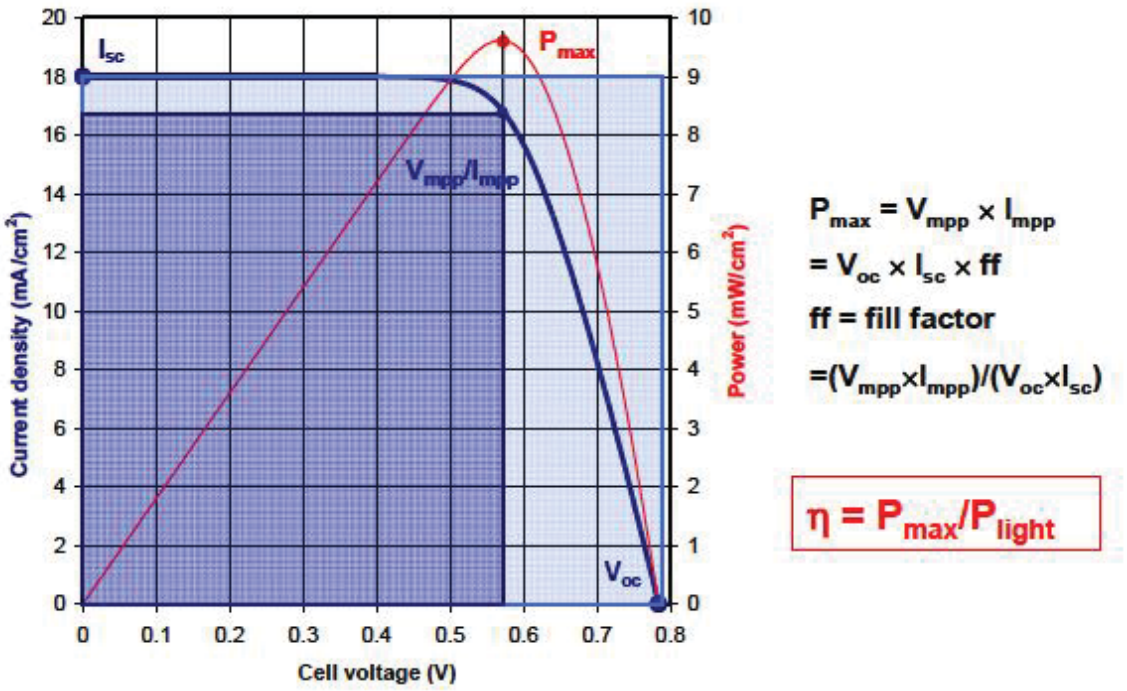

Figure 2.4: I-V and P-V Curves [Desilvestro, 2008]

The photovoltaic cells must be characterized with many different levels of irradiance to find how the maximum power changes as a function of light intensity. It can be shown that the short circuit current of a solar cell will increase proportionately with an increase in irradiance. The open circuit voltage, however, will increase logarithmically. Since the short circuit current is nearly proportional to the incident radiation, it can be used to calculate the incident radiation [Duffie and Beckman, 2006]. This can be useful when the current voltage characteristic can be found but a pyranometer cannot be purchased to properly measure the irradiance.

At each different irradiance level, it is crucial to keep the cell's operating temperature constant. This is due to the temperature effects that will change the I-V curve. To show temperature effects, many different graphs should be made at each temperature, with each graph showing multiple traces of the current voltage characteristic at different levels of irradiance. As can be expected, the maximum power at a given irradiance will decrease as the cell's operating temperature is increased.

The maximum power point has been known to decrease by as much as 19.5% when increasing the temperature from 20℃ to 50℃. The open circuit voltage can be observed to decrease linearly with an increase in temperature [Desilvestro, 2008]. The temperature will typically have an increasing effect on the short circuit current at a rate of +0.05%/℃, while an increase in temperature will decrease the open circuit voltage at a rate of -0.5% ℃. A graph showing this phenomenon is shown in Figure 2.5 ["Part II - Photovoltaic Cell I-V Characterization Theory and LabVIEW Analysis Code"].

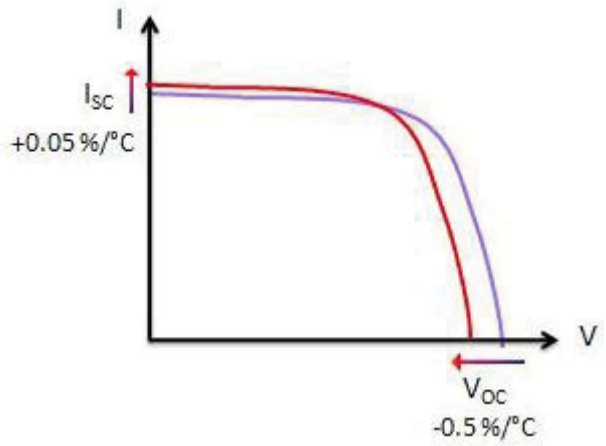

Figure 2.5: Temperature Effect on I-V Curves ["Part II - Photovoltaic Cell I-V Characterization Theory and LabVIEW Analysis Code"]

Values such as open circuit voltage, short circuit current, power generated, maximum power generated, voltage at maximum power, current at maximum power, and fill factor can be found using an I-V curve. Shunt and series resistances can also be approximated using an I-V curve. Losses exist in solar cells due to internal resistances that decrease efficiency. To model these resistances, a shunt resistance in parallel and a series resistance are placed in the solar cell's equivalent circuit, as can be seen in Figure 2.3. For maximum efficiency, the shunt resistance should be as high as possible, with the series resistance kept at a minimum. These can be approximated on the I-V curve by taking the slope of the two main portions of the curve. The shunt resistance can be estimated as the inverse of the slope of the leftmost part

of the I-V curve (at the short circuit current), while the series resistance is found from the inverse of the slope of the right portion of the curve (at the open circuit voltage). This will give a better approximation of the shunt resistance. The series resistance, however, will be proportional but smaller than the resistance found at the open circuit voltage ["Part II - Photovoltaic Cell I-V Characterization Theory and LabVIEW Analysis Code"]. A better approximation of the series resistance is the "different illumination level method," which involves using two different I-V curves at different irradiance levels. This method, however, will give errors if the temperature is not kept constant. Methods have been developed to compensate for this, such as the "constant illumination level method." This method keeps the irradiance constant and factors in the temperature change [Ishibashi et al., 2008].

2.5 Scope of Thesis

The rest of this thesis investigates different methods for cooling the surface of solar panels in order to prevent the conversion efficiency from diminishing. This was done in three ways. First, analytical equations were found and calculations were performed to find the theoretical temperatures for the case of a bare panel with natural convection. Second, ANSYS was used to run various computational models. Finally, an experiment was setup in an attempt to match the results given computationally and by analytical calculations.

Chapter 3

Analytical Calculations

3.1 Mathematical Model

The equation for this model is derived from the energy equation. The energy equation for this case is a partial differential equation derived from Fourier's law of heat conduction that describes the temperature distribution at any point in space or time. The equation must be solved using known boundary conditions. The basic equation is shown below for a three-dimensional plate [Mossayebi, 1987].

$$\frac{\partial T}{\partial t} - \alpha \left(\frac{\partial^2 T}{\partial x^2} + \frac{\partial^2 T}{\partial y^2} + \frac{\partial^2 T}{\partial z^2} \right) = 0 \tag{3.1}$$

It can be assumed that the temperature variation for this case is steady-state and one dimensional. In this case, the formula simplifies to:

$$\frac{\partial^2 T}{\partial x^2} = 0 \tag{3.2}$$

The general solution to this differential equation can be solved by integrating twice. The result is shown in equation 3.3.

$$T(x) = C_1 x + C_2 \tag{3.3}$$

Equation 3.3 can be solved for C_1 and C_2 by applying the applicable boundary conditions discussed in the next section.

3.2 Boundary Conditions

The problem was first investigated using analytical calculations. Basic heat transfer equations were used to model the solar panel as a plane wall with multiple layers, each with their own thermal properties. Literature research revealed that a typical solar panel is made of layers of glass, EVA, ARC, silicon, and Tedlar [Lee et al., 2008]. The thermal conductivity of these materials was referenced as well as the average thickness of each of the layers.

Two boundary conditions were needed in order to solve the equations to find the temperature at both surfaces of the solar panel. The first set the solar heat flux on the top surface equal to heat conduction throughout the panel and heat that escapes the surface by convection. The second boundary condition set heat conduction equal to the heat convection at the back surface of the panel. The subscript "1" denotes a condition on the front of the panel, while "2" denotes a condition on the back surface. Figure 3.1 shows a schematic of the solar panel modeled as a 2D plane section with the appropriate boundary conditions. These two boundary conditions are shown in the following two equations, respectively.

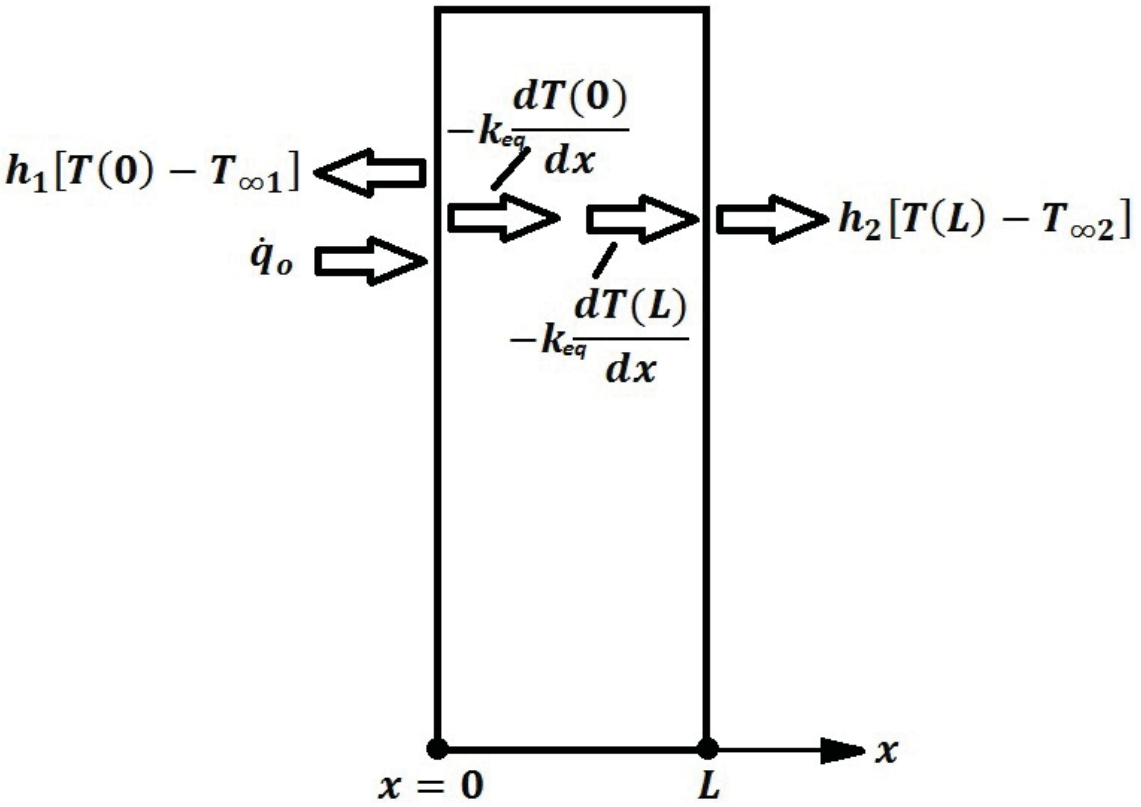

Figure 3.1: Boundary Conditions on Solar Panel

$$-k_{eq}\frac{dT(0)}{dx} = \dot{q}_o - h_1[T(0) - T_{\infty 1}] \tag{3.4}$$

$$-k_{eq}\frac{dT(L)}{dx} = h_2[T(L) - T_{\infty 2}] \tag{3.5}$$

The differential equation was solved symbolically and yielded the following results:

$$T(0) = \frac{h_1 h_2 L T_{\infty 1} + \dot{q} h_2 L + h_1 k T_{\infty 1} + h_2 k T_{\infty 2} + \dot{q} k}{h_1 k + h_2 k + h_1 h_2 L} \tag{3.6}$$

$$T(L) = \frac{h_1 h_2 L(T_{\infty 2} - T_{\infty 1}) - \dot{q} h_2 L + h_1 h_2 L T_{\infty 1} + \dot{q} h_2 L + h_1 k T_{\infty 1} + h_2 k T_{\infty 2} + \dot{q} k}{h_1 k + h_2 k + h_1 h_2 L} \tag{3.7}$$

These equations were backsolved to find the convective heat transfer coefficient. However, it was assumed that the "h_2" in the above equations was actually a com-

bined heat transfer coefficient that included both convective and radiative effects ($h_{combined} = h_{conv} + h_{rad}$). To compensate for this, the radiation value was calculated and subtracted out by first assuming that the surface temperature under the panel (to which the radiation was transfered to) was equal to the ambient temperature. This required finding h_{rad} through the following relation:

$$h_{rad}(T_s - T_{surr}) = \epsilon\sigma(T_s^4 - T_{surr}^4) \tag{3.8}$$

Once the radiative heat transfer coefficient was found, it was subtracted from the combined radiation found in the previous equations. This gave a more accurate value to compare to the results found from the calculations performed with experimental data.

3.3 Analytical Results

Equations 3.6 and 3.7 were both solved using heat transfer coefficients found from the experimental calculations. Because of the complexity of analytical calculations for finned surfaces, these equations only applied to the bare panel with natural convection. The assumption was made that the ambient temperature on both sides of the panel was 22℃. Table 3.1 shows the calculated temperatures for a bare panel with natural convection.

Table 3.1: Temperatures for Bare Panel with Natural Convection

I $\left(\frac{W}{m^2}\right)$	T(0) (℃)	T(L) (℃)
1000	169.53044	165.66324
1250	204.18797	199.29633
1500	247.45344	241.76036

3.4 Atmospheric Conditions

In order to demonstrate the conditions for a worst-case scenario, the atmospheric conditions were chosen in this section to model Phoenix, Arizona. The maximum air temperature in the summer months in Phoenix was found to be 41.06℃[“Climate Data Summary”]. From a map showing the irradiation distribution throughout the United States, the average heat flux (available to photovoltaics) acting upon the top surface of the solar panel was estimated to be $6.8\frac{kWh}{m^2 \cdot day}$ or $283.33\frac{W}{m^2}$ [Roberts, 2008]. A map showing the solar irradiation distribution throughout the United States is shown Figure 3.2.

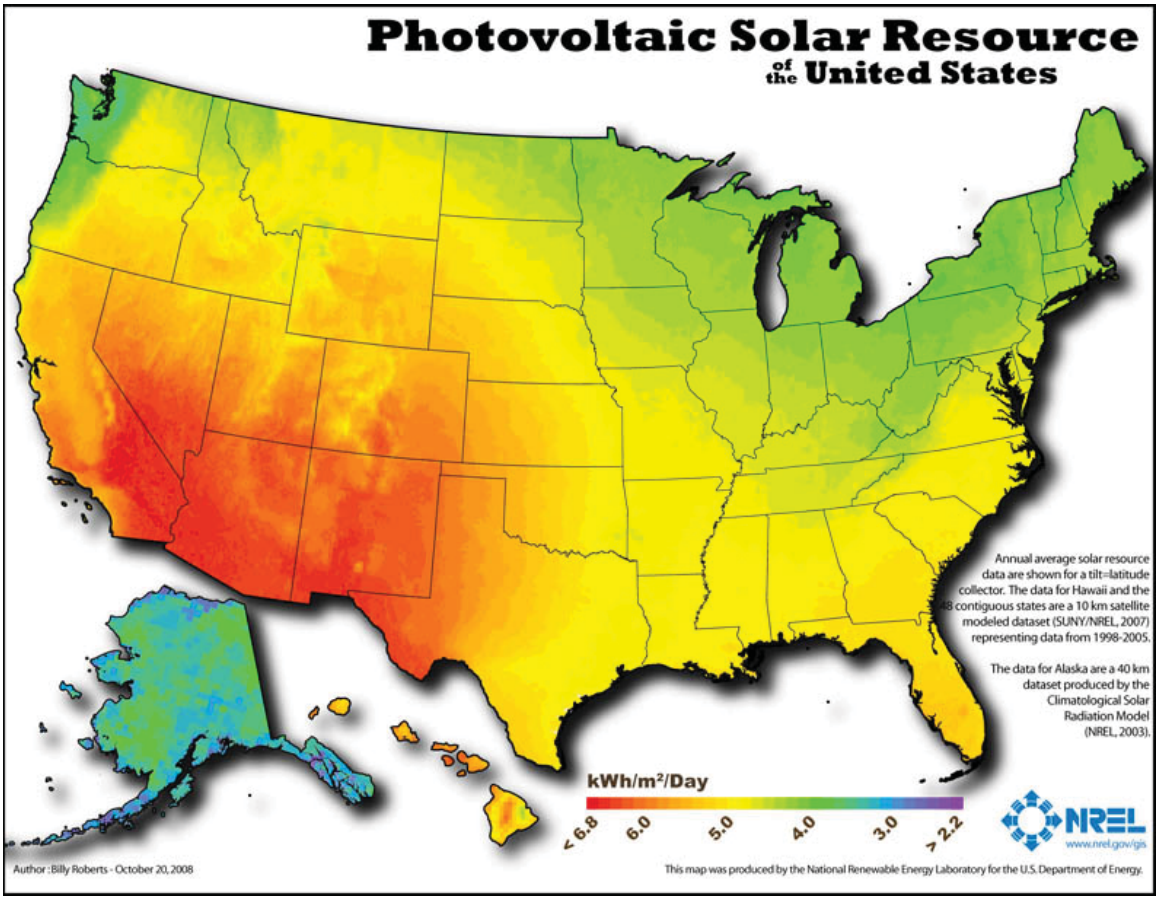

Figure 3.2: Map Showing Solar Irradiation in the U.S. [Roberts, 2008]

However, the daily average factors in non-peak hours, including hours after sunset when irradiance is virtually nonexistent. The peak irradiance acting on the solar panel would likely be much higher. The standard irradiance used for solar experiments is considered to be $1000\frac{W}{m^2}$, which is assumed to be in ideal conditions [AL-Sabounchi, 1998]. This irradiance assumption was verified for Phoenix, Arizona by using the ASHRAE Clear Sky Model. The total irradiance, assuming a horizontal panel, is calculated using Equation 3.9:

$$G_t = G_{ND} + G_d + G_R \tag{3.9}$$

where G_t equals total irradiance, G_{ND} equals normal direction irradiation, G_d equals direct radiation (adjusted for clearness), and G_R equals reflected radiation incident on the surface. Since this example uses a horizonal solar panel, G_R will be equal to zero and drops out of the equation. This is due to the view factor from the ground to the solar panel being zero, meaning it will not reflect any radiation onto the top of the panel. In order to calculate normal direction irradiation, many other values must be found first. These values include apparant solar irradiation at air mass equal to zero (A), atmospheric extinction coefficient (B), solar altitude (β_{sol}), clearness number (C_N), sun declination (δ), hour angle (h), and the latitude of the location (l). Direct radiation is then calculated using normal direction irradiation (G_{ND}) and the ratio of diffuse irradiation on a horizonal surface to direct normal irradiation (C). These values found from tables (chosen for the peak day of July 21st) and the calculations are shown in detail [McQuiston et al., 2005].

$$A = 1093\frac{W}{m^2}$$

$$B = 0.186$$

$$C = 0.138$$

$$l = 33.43^\circ$$

$$h = 0, solarnoon$$

Equation 3.10 is used to find a value used in the equation for declination. The value "n" is the day of the year. To match with the data found from tables, July 21st was chosen (day 202).

$$N = (n-1)(260/365) \tag{3.10}$$

$$\begin{aligned}\delta = {} & 0.3963723 - 22.9132745\cos N + 4.0254304\sin N - 0.3872050\cos 2N \\ & + 0.05196728\sin 2N - 0.1545267\cos 3N + 0.08479777\sin 3N\end{aligned} \tag{3.11}$$

$$\beta_{sol} = sin^{-1}[\cos 1\cos\delta\cos h + \sin l\sin\delta] \tag{3.12}$$

$$G_{ND} = \frac{A}{exp\left(\frac{B}{\sin\beta_{sol}}\right)} \tag{3.13}$$

$$G_d = CG_{ND} \tag{3.14}$$

When the numerical values for G_{ND} and G_d were substituted into equation 3.9, the total irradiation was found to be $925.0598\frac{W}{m^2}$. This value is close to the standard value of $1000\frac{W}{m^2}$.

3.5 Experimental Calculations

Once the speed of the wind and the steady state temperatures were found in each experimental case, the convection heat transfer coefficient was calculated. The equations used for finding the heat transfer coefficient were different for each case. These included external forced convection on a flat plate, natural convection on a flat plate, external forced convection on a finned surface, and natural convection on a finned surface. These calculations are shown in more detail in the following sections.

3.5.1 External Forced Convection Over a Flat Plate

This calculation was performed for the case with wind blowing across the back of the bare panel. First, the film temperature was found by calculating the average temperature between the back surface and the ambient air. Once it was assumed that the ambient pressure was 1 atm, the properties of air were found in tables in *Heat and Mass Transfer: Fundamentals & Applications*, by Yunus A. Çengel and Afshin J. Ghajar. These values included the thermal conductivity, Prandtl number, and kinematic viscosity. Then the Reynolds number was calculated using the wind velocity, panel length, and kinematic viscosity:

$$Re_L = \frac{V L_{panel}}{\nu} \tag{3.15}$$

This number was then referenced to the critical Reynolds number of $5X10^5$. For the experiments performed, the Reynolds number was found to be less than the critical number; therefore, the flow was assumed to be laminar. The Nusselt number for a laminar case was then calculated as follows:

$$Nu_x = 0.453 Re_x^{0.5} Pr^{1/3} \tag{3.16}$$

Since this is the local Nusselt number, the local convection heat transfer coefficient was found as follows:

$$h_x = \frac{k}{L_{panel}} Nu \tag{3.17}$$

However, the average heat transfer coefficient needed to be determined. This required the equation to be integrated over the length of the entire backing. This calculation is shown in Equation 3.18.

$$\bar{h} = \frac{1}{L_{panel}} \int_0^{L_{panel}} h_x \, \mathrm{d}x = \frac{0.906 k Pr^{1/3}}{L_{panel}} Re_L^{0.5} \tag{3.18}$$

3.5.2 Natural Convection Over Flat Plate

These next calculations were used to find the convective heat transfer coefficient for the bare back surface of the solar panel with still air, as well as the top of the solar panel in all cases. Once again, the process started with finding the film temperature using the average between the ambient temperature and the measured temperature of the panel. The thermal conductivity, Prandtl number, kinematic viscosity, and coefficient of volume expansion ($\beta = \frac{1}{T_{film}}$) were also used. The next step was to find the Rayleigh number using Equation 3.19, which is a measure of the relationship of buoyancy and viscosity of the fluid [Çengel and Ghajar, 2011].

$$Ra_L = \frac{g\beta(T_s - T_\infty)L_c^3}{\nu^2} Pr \tag{3.19}$$

Equation 3.19 makes use of the characteristic length, which is a ratio of the surface area of the plate and perimeter:

$$L_c = \frac{A_s}{p} \tag{3.20}$$

From the Rayleigh number, the Nusselt number used to find the convective heat transfer coefficient was found for the case of $10^4 < Ra_L < 10^7$.

$$Nu = 0.54 Ra_L^{1/4} \tag{3.21}$$

Finally, the heat transfer coefficient was found from the relation used previously:

$$h = \frac{k}{L_c} Nu \tag{3.22}$$

3.5.3 Forced Convection Across Fins

The following method for finding the Nusselt number for forced convection across fins was developed by Teertstra et al. The calculation for forced convection across fins starts with finding the Reynolds number. Unlike the forced convection over a flat plate calculation, which uses the plate length in the Reynolds number calculation, Equation 3.23 uses the distance between the fins, S_{fin}.

$$Re_L = \frac{V S_{fin}}{\nu} \tag{3.23}$$

The Reynolds number is then non-dimensionalized using the ratio between the channel width, S_{fin}, and the fin length, L_{fin}. This gives the Reynolds number for channel flow.

$$Re_b^* = Re_L \cdot \frac{S_{fin}}{L_{fin}} \tag{3.24}$$

Finally, the Nusselt number for flow between plates was found using Equation 3.25. Included in the equation is combination parameter, n. This number must be optimized (usually to the closest integer) in order for the equation to produce accurate results [Teertstra et al., 2000].

$$Nu_b = \left[\left(\frac{Re_b^* Pr}{2} \right)^{-n} + \left(0.664 \sqrt{Re_b^*} Pr^{\frac{1}{3}} \times \sqrt{1 + \frac{3.65}{\sqrt{Re_b^*}}} \right)^{-n} \right]^{-1/n} \tag{3.25}$$

3.5.4 Natural Convection on Fins

Natural convection across fins was calculated in a similar manner to the calculation for natural convection from the bottom of a flat plate. After the relevent properties are found at the film temperature, the Rayleigh number was once again found using Equation 3.19. The Nusselt number was then found as follows:

$$Nu = 0.27 Ra_L^{1/4} \tag{3.26}$$

This was used to find the Nusselt number for an inclined plate at $0 \leq \theta \leq 45°$.

$$\bar{Nu}_s = 0.645 [Ra_s (S_{fin}/L_{fin})]^{1/4} \tag{3.27}$$

The heat transfer coefficient was then found from the common relation in Equation 3.17.

Chapter 4

Computational Analysis

4.1 ANSYS

To verify the analytical results found, ANSYS was used to model the heat transfer throughout the solar panel. ANSYS is a suite of computer software applications used to perform computer simulations for various cases (e.g., fluid flow, harmonic response, rigid dynamics, etc.) The various programs contained within ANSYS were accessed from ANSYS Workbench, which works as a connecting point between them. The computational analysis was performed for each individual case, using different settings and one of two sub-programs within ANSYS. The sub-programs used (and accessed using Workbench) were ANSYS Mechanical and ANSYS Fluent.

4.1.1 ANSYS Mechanical

For steady-state heat conduction through a plane wall, a two-dimensional model was made for the sake of simplicity. This analysis excluded the need for fluid flow analysis because the still air and heat flux boundary condition left only the temperature distribution through the solar panel to be investigated. Due to these simplified criteria, ANSYS Mechanical was chosen for the case of a bare panel with only natural

convection.

ANSYS Mechanical is primarily a finite element analysis program used to perform static or dynamic analyses on linear and nonlinear structural systems. However, it can also perform a thermal analysis, as well as physics computations with systems such as piezoelectrics ["ANSYS Mechanical"]. For the bare panel with natural convection, only the thermal analysis was performed.

4.1.2 ANSYS Fluent

In addition to the bare panel with natural convection, three other cases were analyzed: (1) bare panel with forced convection and fins with both (2) natural and (3) forced convection. A fluid flow analysis was required for each of these cases. For both cases of forced convection, the fluid flow was modeled for the air flowing underneath the solar panel. For natural convection with fins, fluid flow was not necessarily needed as the air velocity was zero. However, a three-dimensional model was created for each case due to the more complicated nature of fluid flow and fins. The natural convection case was analyzed by modifying the forced convection over fins case by simply changing the air speed to zero. These cases are best analyzed using ANSYS Fluent, a finite volume analysis program.

Ansys Fluent is software included in the ANSYS suite that is used to perform computational fluid dynamics (CFD) analyses. This includes wind over an airfoil, flow through a pipe, etc. The motion of the fluid is calculated as well as the heat transfer (which gives the temperature distribution) and turbulence ["ANSYS Fluent"].

4.2 Bare Panel, Natural Convection, 2D

First, ANSYS Workbench was opened. The correct analysis system was then chosen to be "Steady-State Thermal (ANSYS)" which creates a project file appropriate

for the model that was needed. Then the setup for the model began by adding in the materials and specifying their properties (specifically, thermal conductivity). Table 4.1 shows the thickness and thermal conductivity for each layer [Lee et al., 2008].

Table 4.1: Conductivity and Thickness of Solar Panel Layers

Material	Conductivity ($\frac{W}{m \cdot K}$)	Thickness (m)
Glass	0.98	0.003
EVA1	0.23	0.0005
ARC	1.38	0.08×10^{-6}
Si	148	0.000325
EVA2	0.23	0.0005
Tedlar	0.36	0.0001

The geometry was then created using ANSYS DesignModeler, the computer-aided design (CAD) program used by ANSYS. An arbitrary length of 10 millimeters was chosen for the length of the panel, as the heat transfer is assumed to only be across the thickness. The different layers however were made to have the thicknesses that are typical of common solar panels, as shown in Table 4.1. Due to a minimum length value imposed by DesignModeler, the layer of ARC was omitted from the geometry due to its thickness of 0.08×10^{-3} mm. Therefore, the assumption was made that the effects of this layer were negligible, as its thermal resistance is extremely miniscule in comparison to the solar panel's total resistance. A portion of the geometry created is shown in Figure 4.1.

The next step in the computational analysis was to break up the geometry into elements in a process called "meshing." This was completed using ANSYS Mechanical, a finite element analysis (FEA) application that allows the user to perform structural, thermal, thermoelectric, acoustic, and piezoelectric analyses ["ANSYS Mechanical"]. A rectangular mesh was created, with each layer being divided up into even smaller components. ANSYS Mechanical was also used to add the boundary conditions. A heat flux was added to the outer layer consisting of glass. Natural convection was then applied to the outside layer consisting of Tedlar, and the ends of the layers were

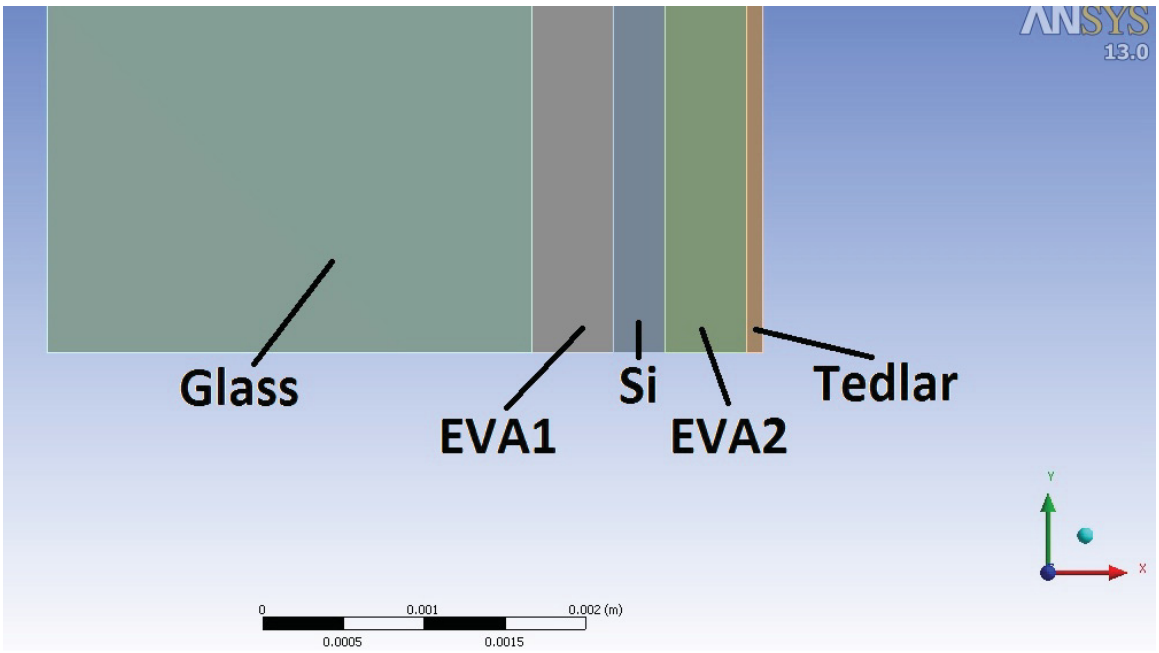

Figure 4.1: Bare Panel Model Created in ANSYS

insulated in order to ignore heat transfer from the sides. Natural convection was also added to the glass layer. Ambient temperatures were assumed to be around room temperature at 22℃, in order to match the conditions in the experimental setup. The heat transfer coefficients for natural convection were taken from calculations from the experimental data. The meshed model is shown in Figure 4.2.

The model was then solved, and results were given in the form of a model showing the temperature distribution throughout the solar panel. The top layer of the solar panel, which is made of glass and exposed to solar radiation, was found to have a steady-state temperature of 168.35℃ when a heat flux of $1000\frac{W}{m^2}$ was applied. The bottom surface, which consists of Tedlar and experiences natural convection, had a temperature of 166.8℃. Figure 4.3 shows the temperature distribution throughout the solar panel.

The results obtained in the computational analysis were consistent with results found using analytical calculations. The found temperatures of the top surface (glass) had a percentage difference of 0.699% for $I = 1000\frac{W}{m^2}$. The percentage difference for

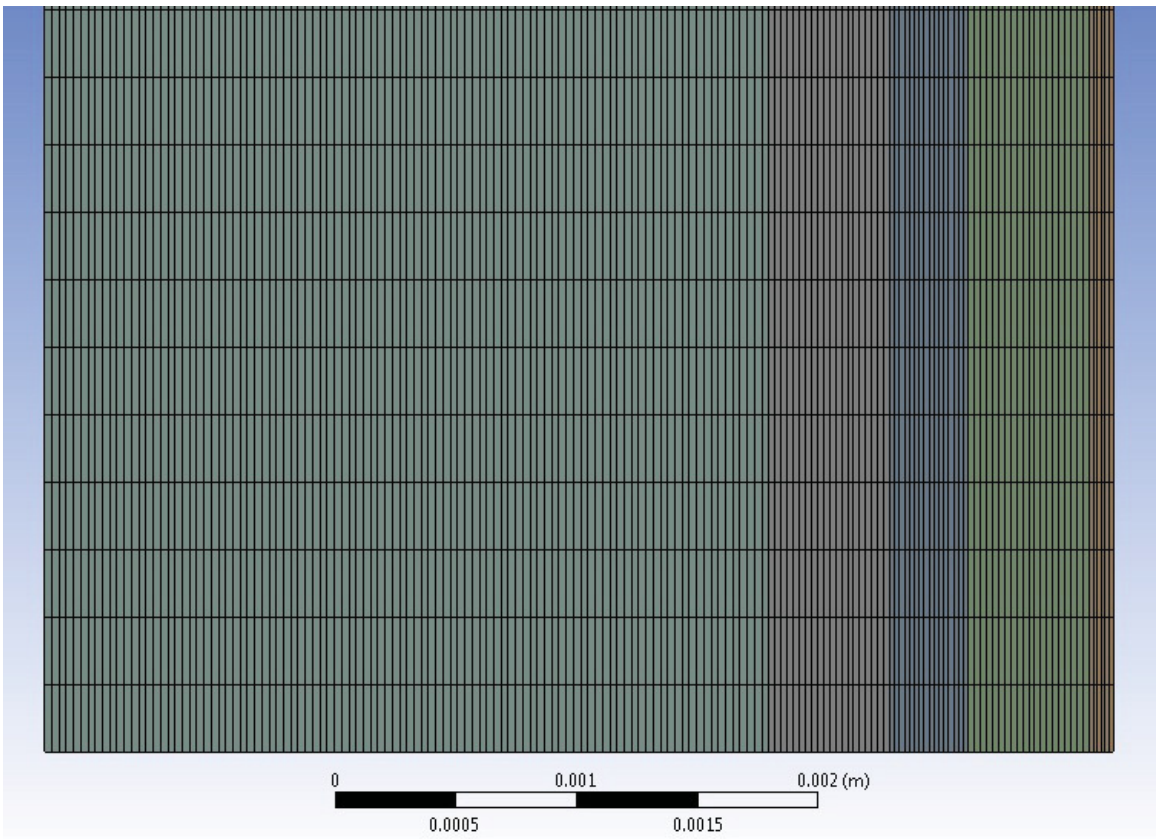

Figure 4.2: Meshed 2D Model

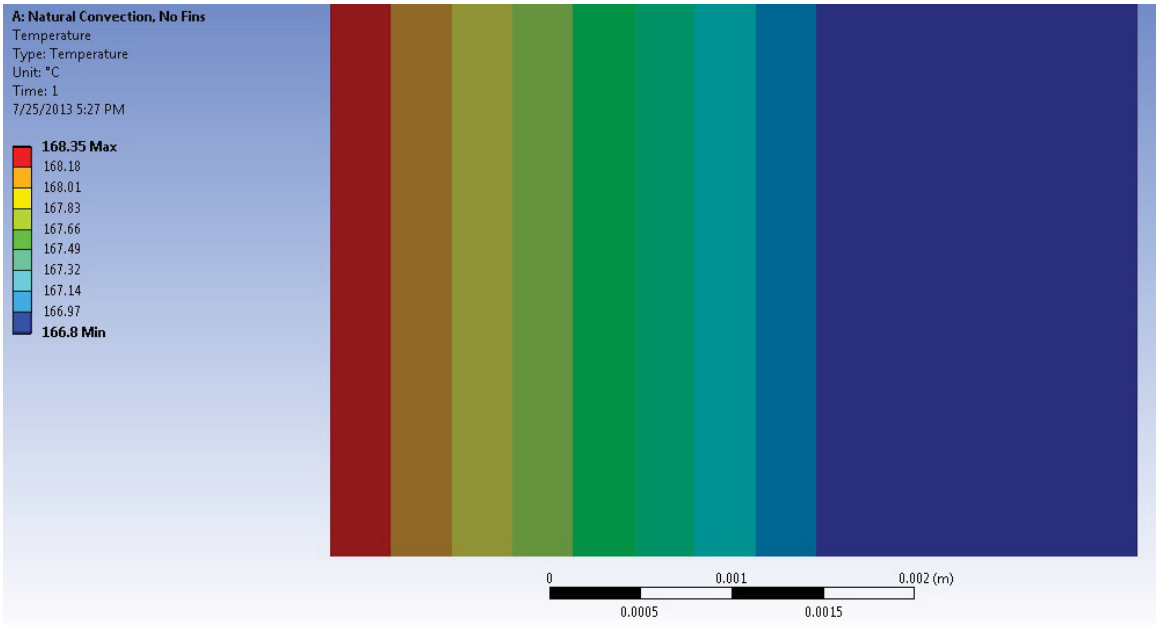

Figure 4.3: Temperature Distribution Throughout Bare Solar Panel with Natural Convection, I = $1000\frac{W}{m^2}$

the bottom surface was 0.684% for the same irradiance. Any small differences could exist because the computational model didn't contain the layer of ARC. Also, the assumption was made that the temperature distribution was uniform throughout the length. In reality, the temperature would slightly vary as the heat transfer approaches the edges. For further assurance, the model was resolved with an even finer mesh. The final temperature distribution remained the same. It was then safely assumed that the results had converged.

Table 4.2 shows the temperatures at the glass (T(0)) and back of Tedlar (T(L)) for each irradiance.

Table 4.2: Bare Panel, Natural Convection Computational Data

I $\left(\frac{W}{m^2}\right)$	T(0) (℃)	T(L) (℃)
1000	168.35	166.8
1250	202.68	200.71
1500	245.75	243.46

4.3 Bare Panel, Forced Convection, 3D

The first steps for each subsequent case were setup similarly to the analysis for the 2D bare panel with natural convection. The geometry, however, was created using Solidworks. This was used to draw a three-dimensional model adhering to the exact specifications of the solar panel dimensions. An extra section was drawn which connects to the backing of the solar panel (i.e., Tedlar). This created a channel through which the air flow could be modeled. The geometry was saved as a parasolid file (extension .x_t) for easy exportation to meshing in ANSYS Mechanical. Figure 4.4 shows the model created in Solidworks, while Figure 4.5 shows a magnified model where the layers (right-to-left: air, glass, EVA layer 1, ARC, Silicon, EVA layer 2, Tedlar) can be seen.

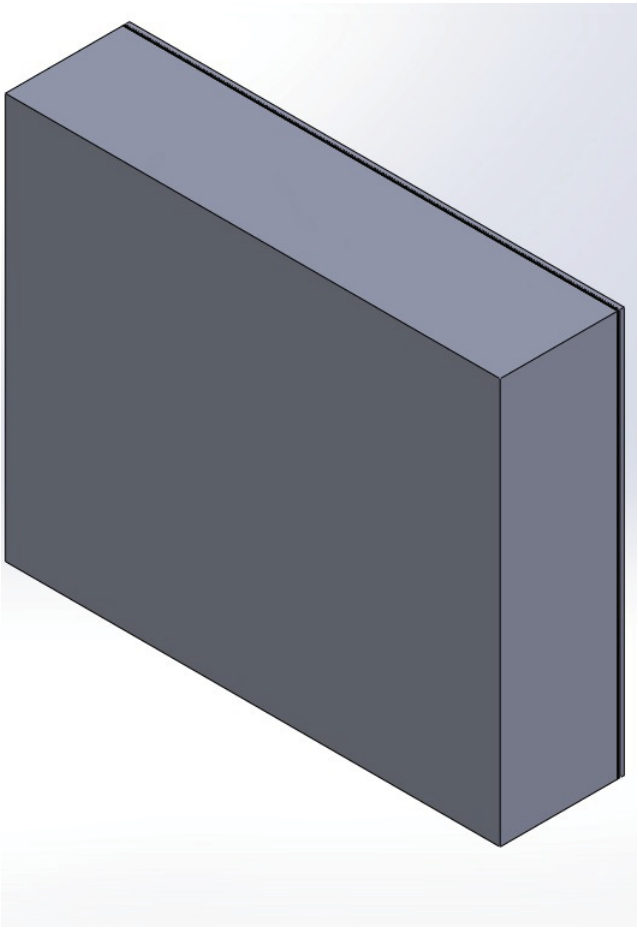

Figure 4.4: Bare Panel Model Created in Solidworks

Figure 4.5: Closeup of Bare Panel Model Created in Solidworks

After the geometry was imported, the next step was to create an efficient mesh. An automatic mesh was created at first. After the next steps were taken and the full analysis was performed, the mesh was updated in an attempt to create more accurate results. This included customizing the mesh by setting the divisions on each edge to a pre-chosen number. Further, midside nodes (which gives each rectangular element 8 nodes for solution points instead of 4) were placed on each model for a second solution. This process was repeated until the results were considered sound, and there was little variation in the final temperature distributions. The meshed bare panel can be seen in Figure 4.6.

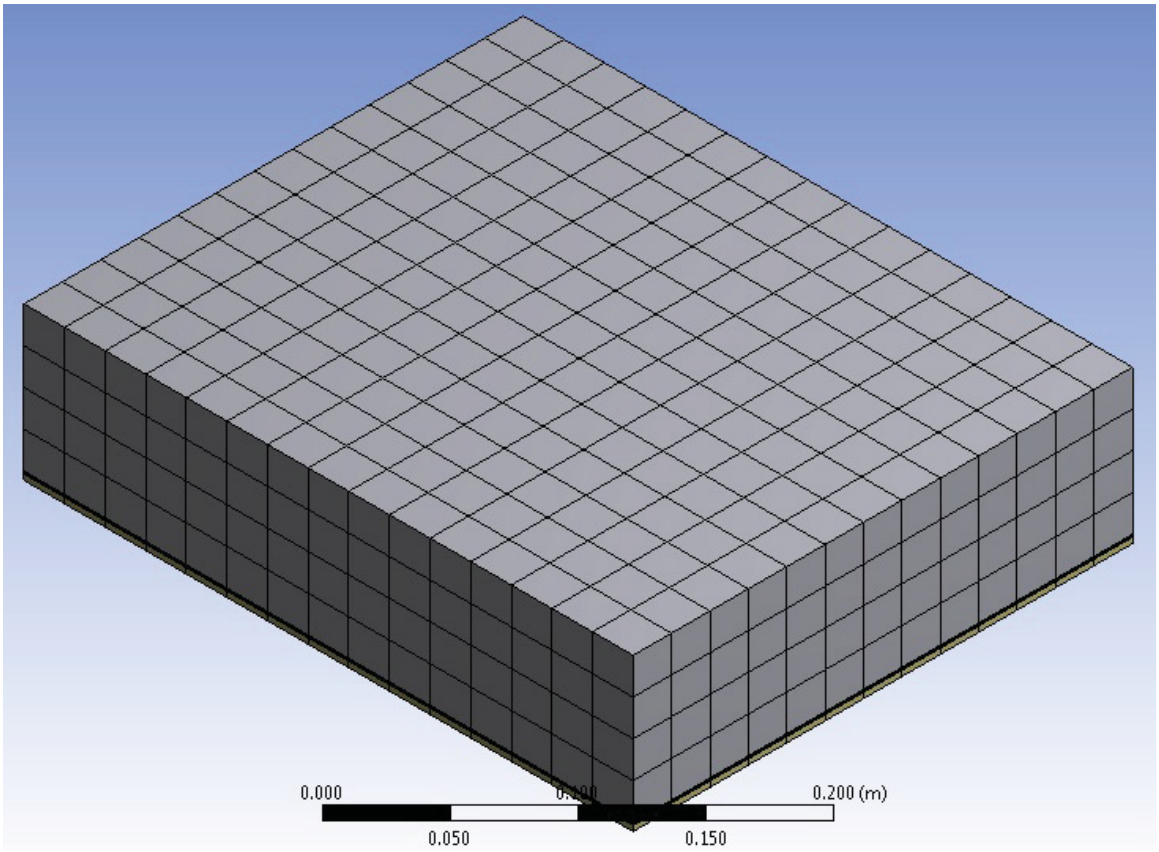

Figure 4.6: Meshed Bare Panel Model

The next step was to open Fluent to calculate a solution. Before loading Fluent, an option was selected called "Double Precision." Although slower to converge, this option can maintain more accuracy in cases with airflow or complicated geometry. Upon opening Fluent, the default setup options were kept aside from turning on the "Energy Equation." This allows for heat transfer to be calculated throughout the solar panel. The next step was to add the materials and their thermal conductivities. Each geometrical body was then selected and correlated with its proper material. Boundary conditions were then set for the glass top (heat flux, which models the irradiance) and the inlet/outlet of the air channel. The temperatures for the inlet and outlet were set to the ambient temperature of 299 K. The outlet was set as a pressure outlet, which allows outflow caused by a velocity of a fluid coming through the inlet. Finally, the velocity was set at the inlet. Mesh interfaces were then created at each interface between the different materials. This tied two walls into one, which allowed heat flow to travel across the materials without hitting an infinitely small gap. The solution was then initialized and run. Residuals were modeled, such as energy (convergence criteria = 1e-0.6), continuity (convergence criteria = 0.001), and velocity (convergence criteria = 0.001). Once the residuals converged, the calculation was complete and temperature distributions could be viewed after opening the Results section in Workbench. Individual node temperatures at the center of the Tedlar backing (where the thermocouple was adhered during the experimental setup) were checked using the "Probe" tool. This process was repeated for each irradiance at each of the velocities used in the experimental setup. Table 4.3 shows the temperatures at the glass (T(0)) and back of Tedlar (T(L)) for each irradiance. Also, Figure 4.7 shows the temperature distribution for the bare panel, with an irradiance of $1000\frac{W}{m^2}$ and a velocity of $2.54\frac{m}{s}$.

Table 4.3: Bare Panel, Forced Convection Computational Data

I $\left(\frac{W}{m^2}\right)$	V $\left(\frac{m}{s}\right)$	T(L) (℃)
1000	1.12	139.689
1000	1.37	126.758
1000	2.54	102.735
1250	1.12	167.478
1250	1.37	152.176
1250	2.54	122.512
1500	1.12	196.076
1500	1.37	179.541
1500	2.54	140.83

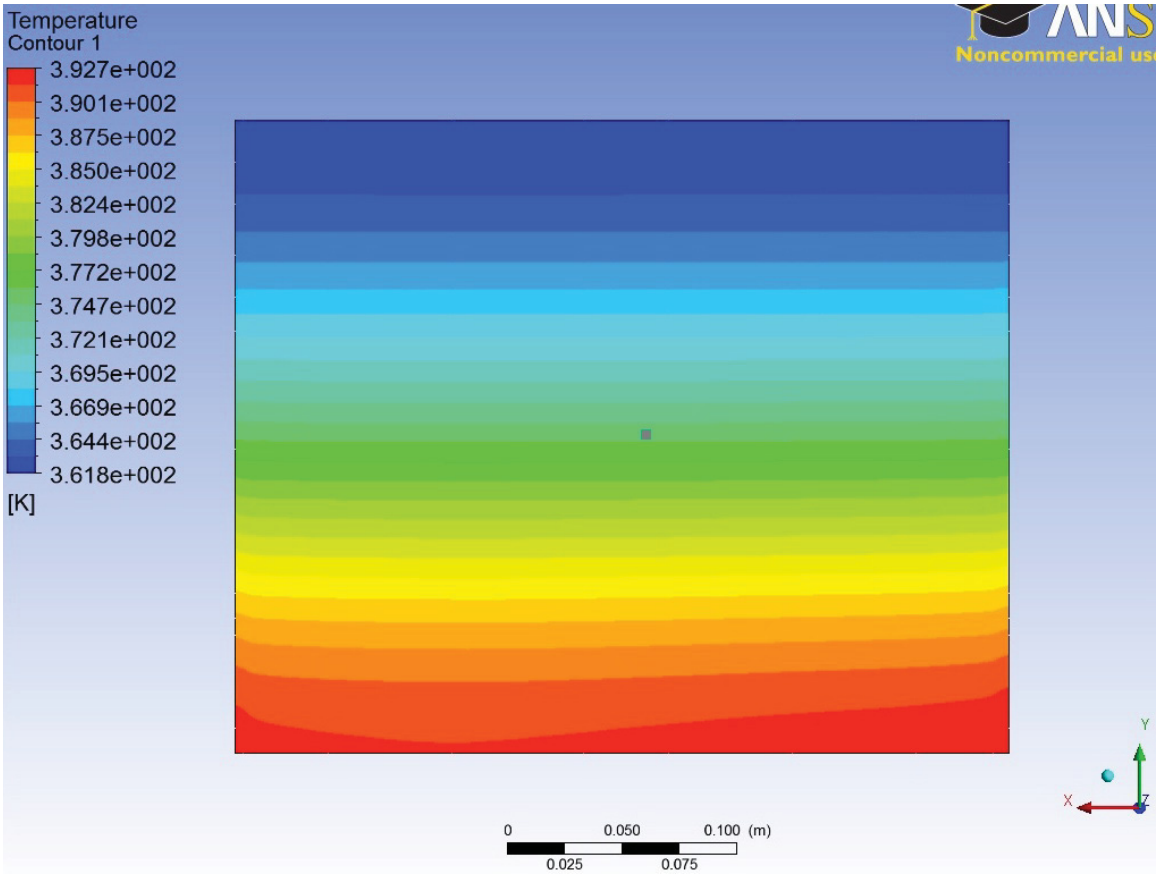

Figure 4.7: Temperature Distribution for Bare Panel, $I = 1000\frac{W}{m^2}$, $V = 2.54\frac{m}{s}$

4.4 Fins, Natural Convection, 3D

The process for the finned solar panel with natural convection model started similar to the previous model. The solar panel and fins were drawn in Solidworks and imported into ANSYS Design Modeler using a parasolid file. The mesh was then created in the

manner discussed previously, which special attention paid to the elements on the fins. The mesh was refined until there was little variation in the temperature distrubition between the different meshes. The models and meshes for each heat sink are shown in Figures 4.8, 4.9, 4.10, and 4.11. Isometric views of Sink 1 and Sink 2 are shown in the Appendix.

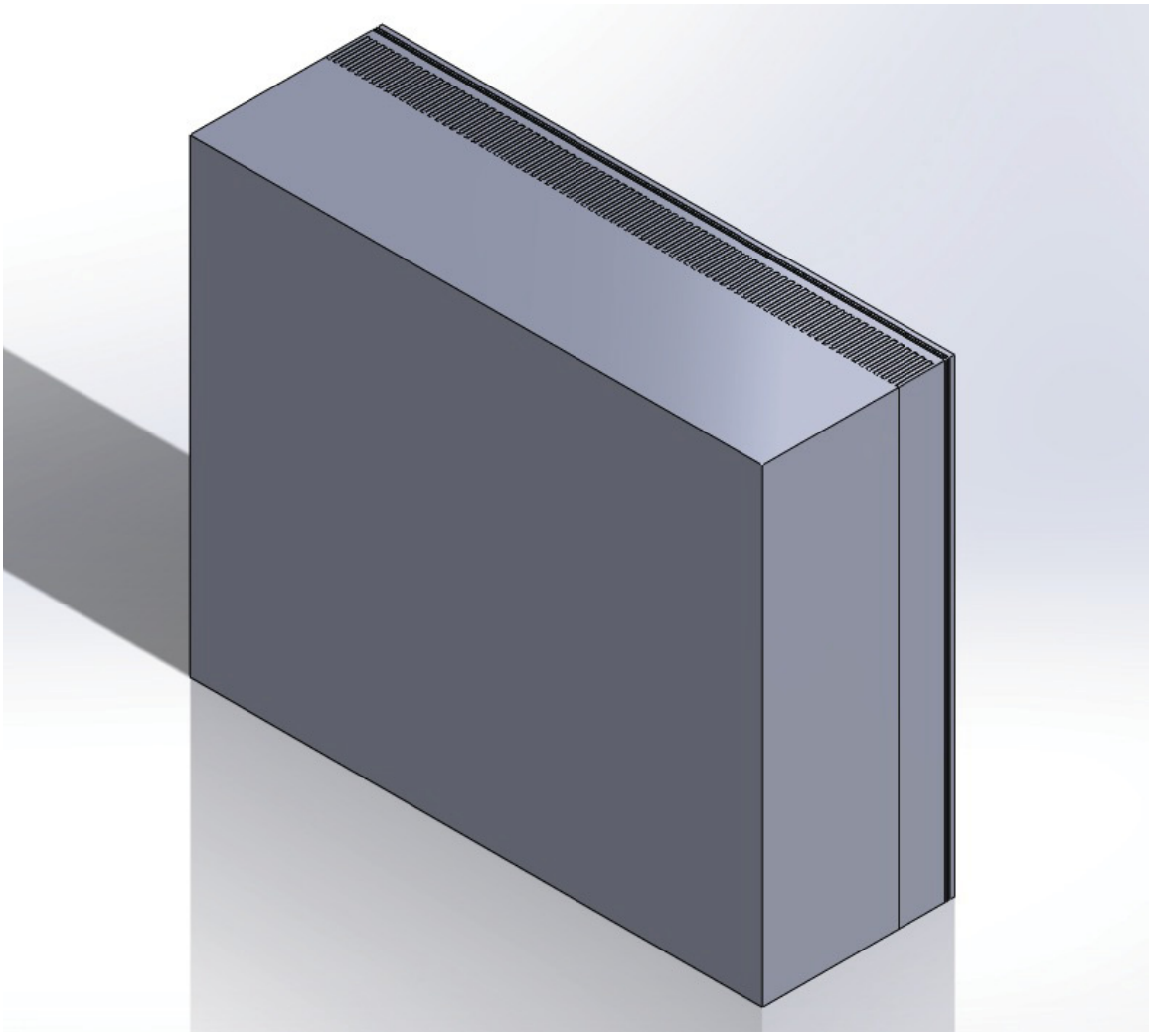

Figure 4.8: Model of Solar Panel with Heat Sink 1

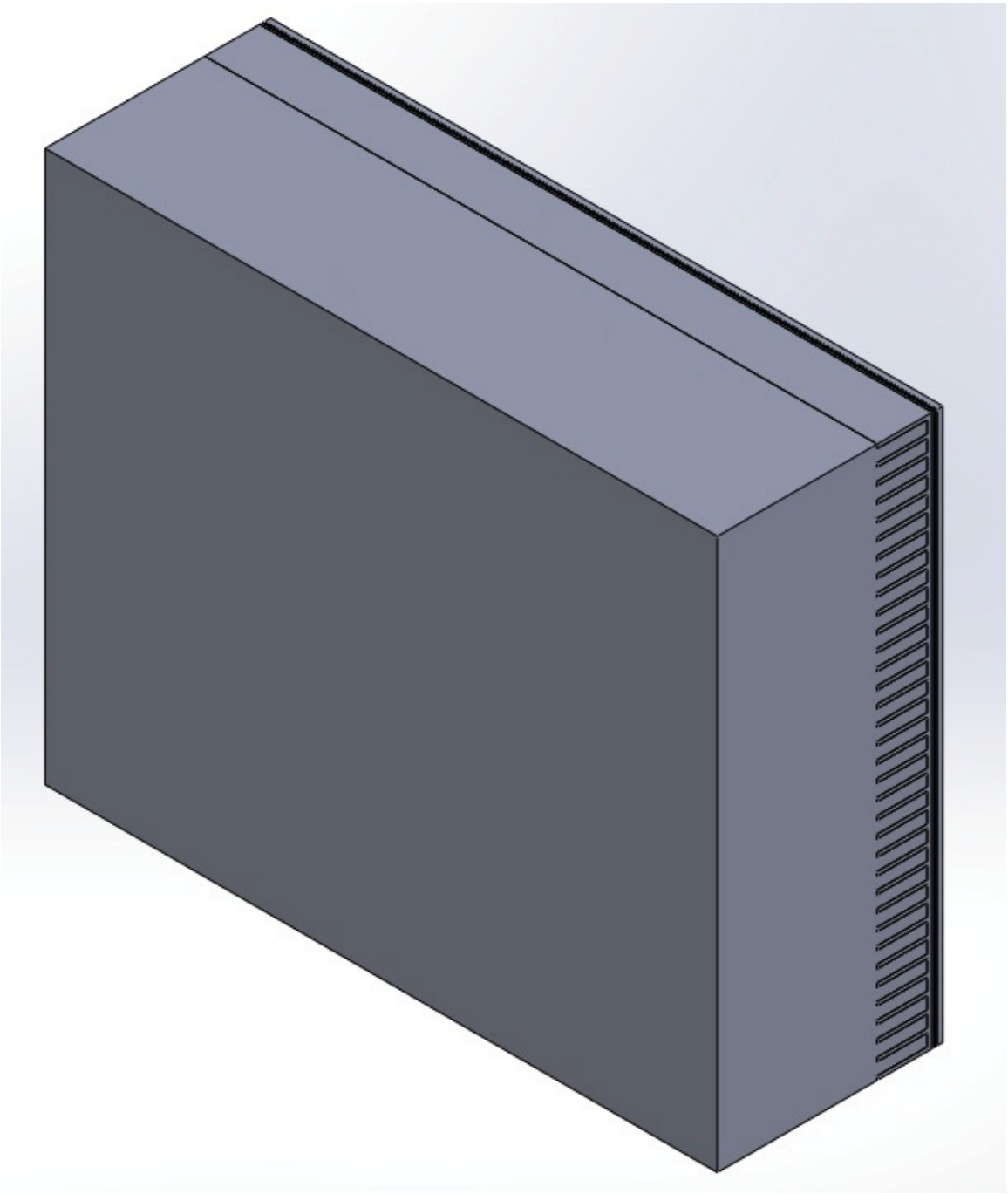

Figure 4.9: Model of Solar Panel with Heat Sink 2

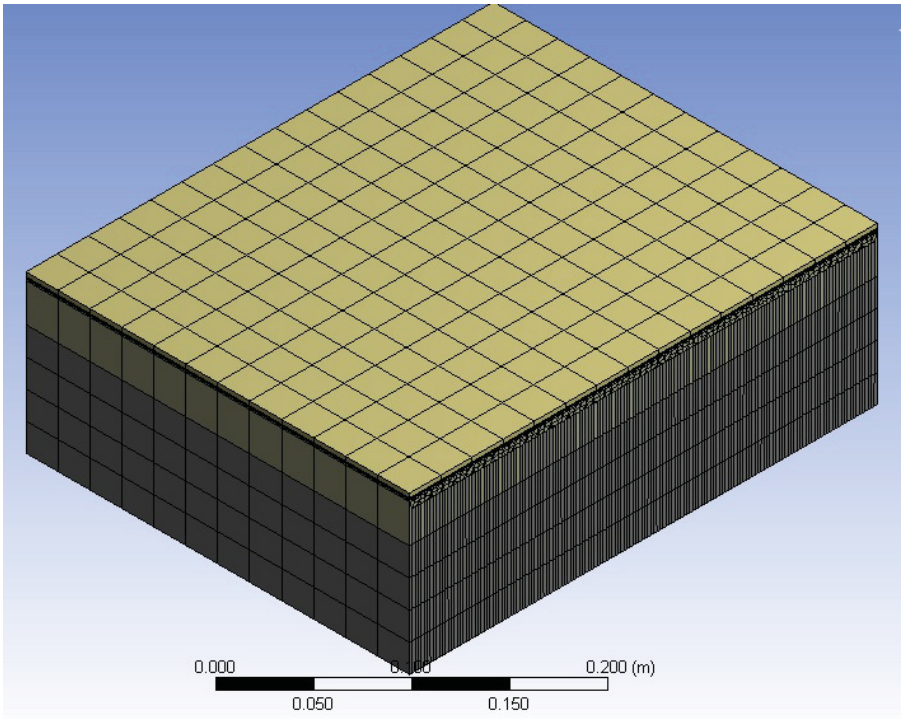

Figure 4.10: Mesh Shown on Sink 1 Model

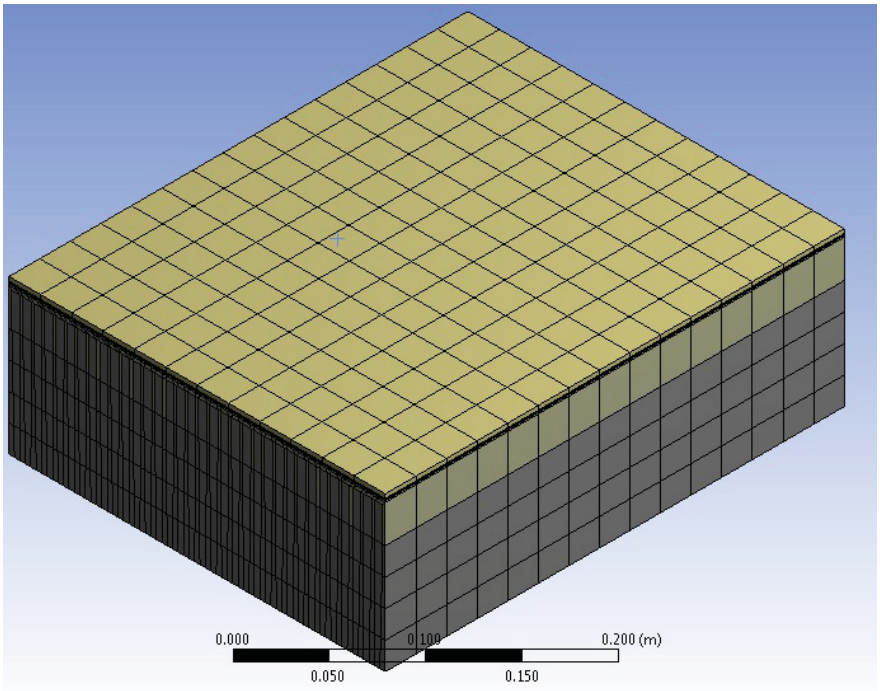

Figure 4.11: Mesh Shown on Sink 2 Model

The setup method was different due to the model having natural convection. As Fluent was opened, "Double Precision" was selected to ensure accuracy. First, gravity was activated and the components were set to mimic the panel being tilted at a 10 degree angle. Then operating conditions were set to keep the air temperature at 299 K and the operating air density at $1.225\frac{kg}{m^3}$. The different materials were then added along with their thermal conductivities. For air, the model differed from forced convection by setting the density option to "boussinesq." This allows Fluent to model bouyancy driven flows with little to no density changes. Also, it was required that a thermal expansion coefficient for air be specified as 0.003407. Under "Solution Methods," the pressure setting was changed to "Second-Order." The boundary conditions were then set to model natural convection, keeping the air temperatures at 299 K and the velocity inlet condition to zero. The model was then initialized and run until converged. This was repeated for each heat sink with each of the three heat flux conditions. Table 4.4 shows the temperatures at the base of the fins for each irradiance, and Figures 4.12 and 4.13 show the temperature distributions for an irradiance of $1000\frac{W}{m^2}$.

Table 4.4: Fins, Natural Convection Computational Data

Heat Sink	I $\left(\frac{W}{m^2}\right)$	T(℃)
1	1000	130.72
1	1250	144.92
1	1500	177.167
2	1000	112.244
2	1250	125.283
2	1500	137.343

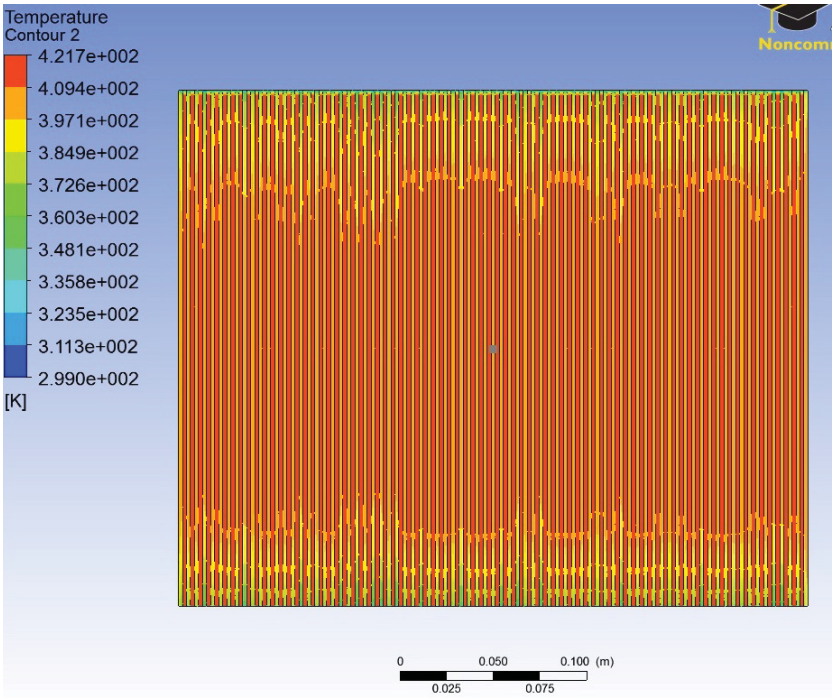

Figure 4.12: Temperature Distribution Throughout Solar Panel with Sink 1 - I = 1000 $\frac{W}{m^2}$, V = 0 $\frac{m}{s}$

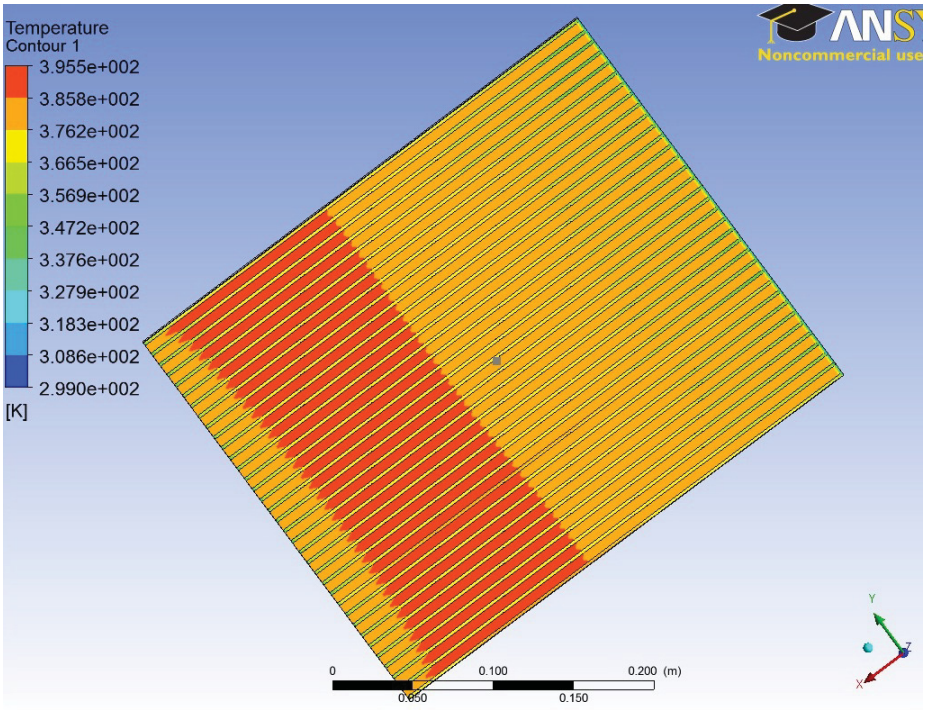

Figure 4.13: Temperature Distribution Throughout Solar Panel with Sink 2 - I = 1000 $\frac{W}{m^2}$, V = 0 $\frac{m}{s}$

4.5 Fins, Forced Convection, 3D

The setup for the finned solar panels with forced convection was identical to the setup for forced convection with the bare panel. The three-dimensional models for the finned solar panels shown previously, as well as the meshes previously shown, were used. The model was run for each air velocity at each irradiance for both finned panels. The temperatures at the base of the fins are shown in Table 4.5 for each irradiance. Figures 4.14 and 4.15 show the temperature distributions for sinks 1 and 2, respectively.

Table 4.5: Fins, Forced Convection Computational Data

Heat Sink	I $\left(\frac{W}{m^2}\right)$	V $\left(\frac{m}{s}\right)$	T(L) (℃)
1	1000	1.12	49.519
1	1000	1.37	45.977
1	1000	2.54	36.793
1	1250	1.12	55.64
1	1250	1.37	51.216
1	1250	2.54	39.518
1	1500	1.12	61.779
1	1500	1.37	56.342
1	1500	2.54	42.225
2	1000	1.12	46.138
2	1000	1.37	42.997
2	1000	2.54	37.937
2	1250	1.12	51.22
2	1250	1.37	47.923
2	1250	2.54	40.784
2	1500	1.12	56.141
2	1500	1.37	52.409
2	1500	2.54	43.771

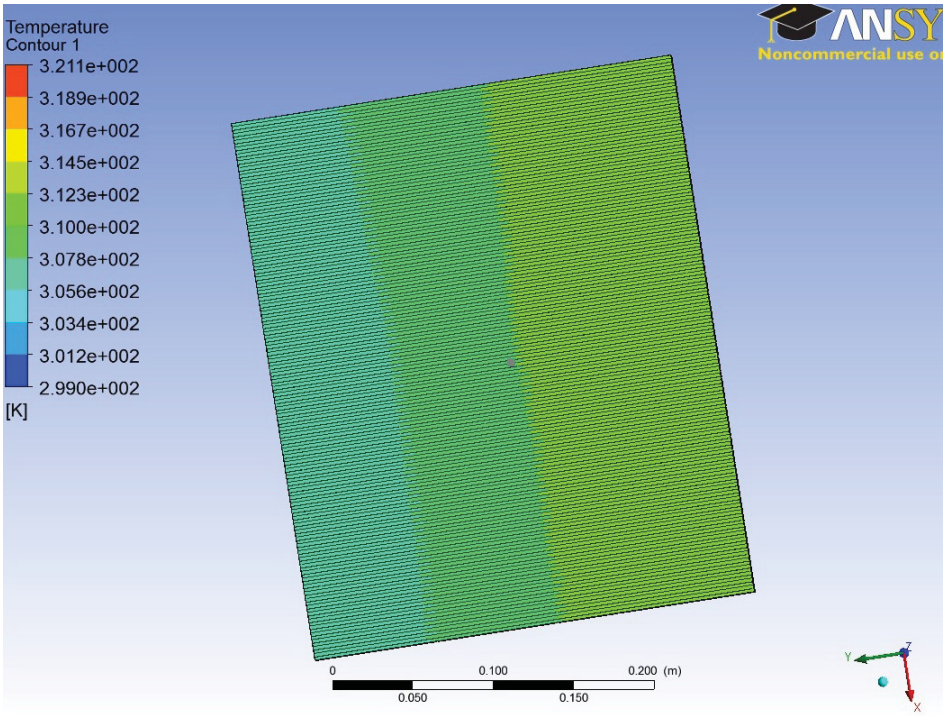

Figure 4.14: Temperature Distribution Throughout Solar Panel with Sink 1 - I = 1000 $\frac{W}{m^2}$, V = 2.54 $\frac{m}{s}$

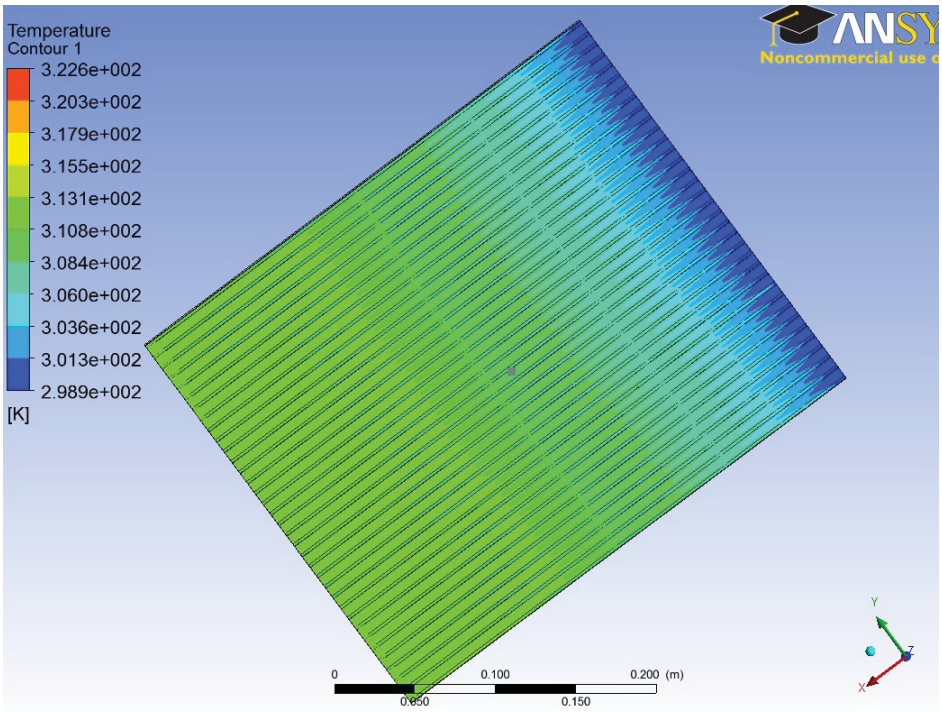

Figure 4.15: Temperature Distribution Throughout Solar Panel with Sink 2 - I = 1000 $\frac{W}{m^2}$, V = 2.54 $\frac{m}{s}$

Chapter 5

Experimental Analysis

5.1 Objective

The main objective of the experimental analysis was to verify the results obtained by analytical calculations and computational methods. Variables in a real-world application can be compensated for in the experimental analysis, while the analytical and computational methods used simplified models and assumptions that gave idealized results.

Care was taken to ensure that the experiment was setup in a uniform manner for each phase of testing. This was required as an assurance that the experiment was repeatable and reliable results could be obtained. New equipment was purchased in order to avoid technical errors and to make certain that the measurement tools were properly calibrated. The basic setup is shown in Figure 5.1. The fan can be seen blowing across the bottom surface of the solar panel, with the panel tilted at 10°. Also shown are the dimensions for the two heat sinks in Figure 5.2.

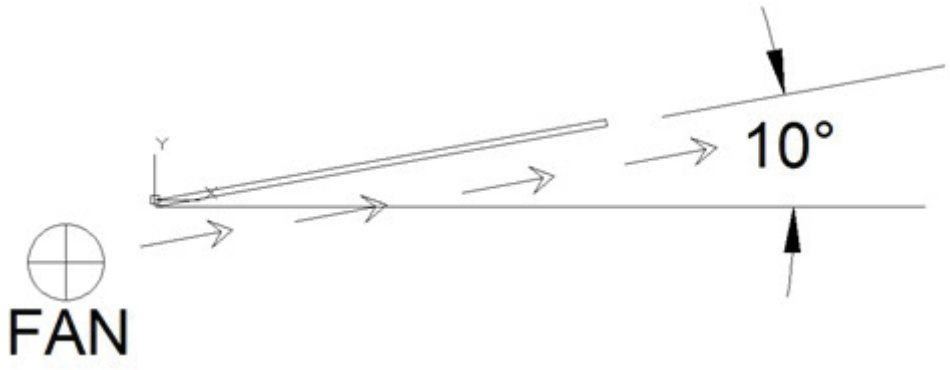

Figure 5.1: Basic Experimental Setup

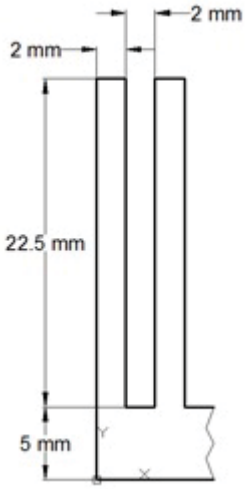

(a) Heat Sink 1. Depth = 0.276m. Length = 0.337m.

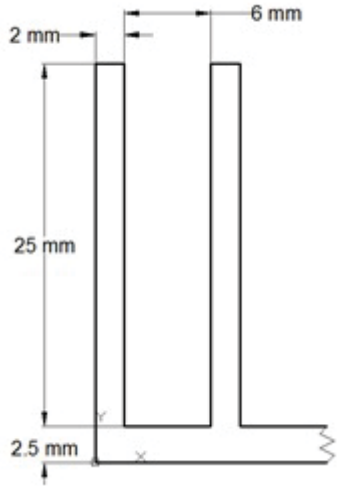

(b) Heat Sink 2. Depth = 0.337m. Length = 0.276m.

Figure 5.2: Dimensions of Heat Sinks

5.2 Apparatus

5.2.1 General

Various equipment was used in the experimental analysis, which included the following: Suntech STBKb 10Watt solar module, NI PXI-4130 Power SMU, NI PXIe-1073 5-Slot 3U PXI Express Chassis with AC plus Integrated MXI-Express Controller, a PC laptop with National Instruments Labview 2011, thermocouple wire, a pyranometer, VelociCalc Plus Multi-Parameter Ventilation Meter 8386, a Holmes Products Corp. electric fan, NI 9219 24-Bit Universal Analog Input Data Acquisition (DAQ) Unit, NI cDAQ 9172 Legacy NI CompactDAQ Chassis, and a custom made box for containing the light given off by 90 Watt halogen flood lights manufactured by General Electric.

Figure 5.3 shows a diagram of the major components used in the experimental setup. Use each section below to reference the component number in the line diagram.

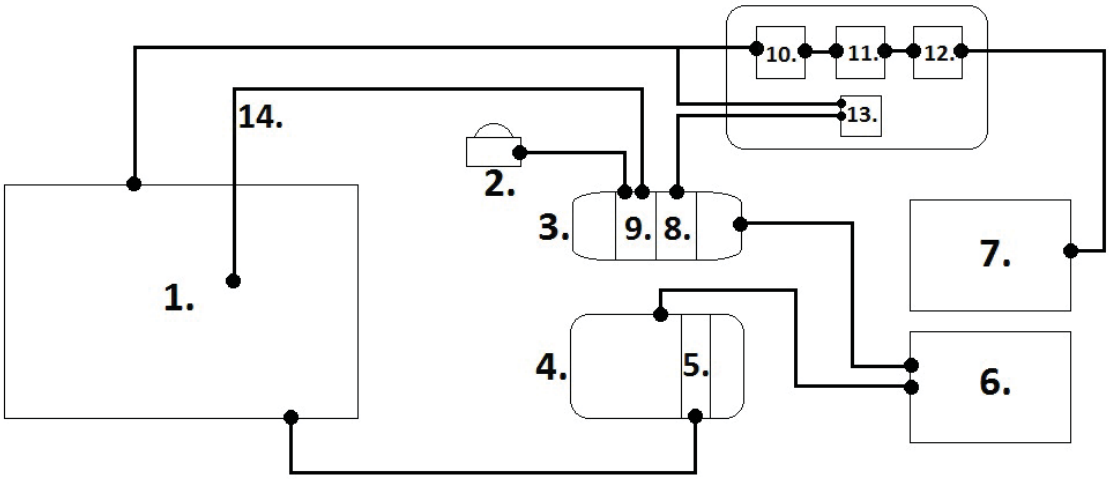

Number	Component		Number	Component
1	Suntech STBKb 10 Watt Solar Module		8	Analog Output Module
2	Pyranometer		9	DAQ
3	DAQ Chassis		10	Dimmer
4	SMU Chassis		11	Servo
5	Power SMU		12	BASIC Stamp HomeWork Board
6	Dell Vostro		13	Relay
7	Dell Latitude		14	Thermocouple Wire

Figure 5.3: Line Diagram of Major Components

5.2.2 Solar Module

A smaller-scale solar panel was used as a representative area of a larger panel used in typical PV cell applications. A Suntech STBKb 10Watt solar module was used, which consists of a 12 by 6 array of PV cells. The panel has dimensions of 14.5in x 12.2in (0.3683m x 0.30988m), with a thickness of 0.70in (0.01778m). The module has a Peak Power Voltage (Vmpp) of 17.4 Volts, and a Peak Power Current (Impp) of 0.57 Amps, which gives a Peak Power (Pmpp) of 10 Watts. The maximum power is achieved during peak hours, assuming a total efficiency of 8.8%. Two panels of the same model were used in order to perform the experiment for two different fin configurations. The solar module is shown in Figure 5.4.

Figure 5.4: Suntech STBKb 10 Watt Solar Module

5.2.3 Pyranometer

A pyranometer manufactured by Kipp & Zonen (model SP Lite2) was used to measure the irradiance given off by the halogen lights. As can be seen in figure 5.5, the pyranometer was attached to a cord which is attached to the DAQ. The irradiance was indicated on a VI made in Labview. The lights were adjusted until the pyranometer measured an irradiance at a specific target value ($1000, 1250, 1500 \frac{W}{m^2}$).

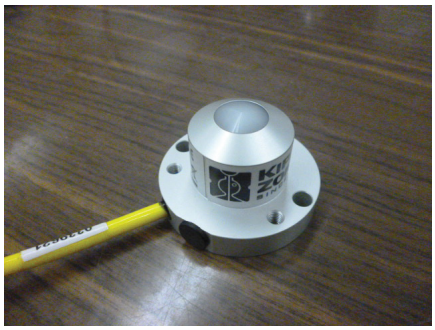

Figure 5.5: Kipp & Zonen Pyranometer

5.2.4 Data Acquisition Unit

In order to obtain data from the experiment, the NI 9219 24-Bit Universal Analog Input Data Acquisition Unit was used. The DAQ acquired temperature data from the thermocouple as well as irradiance from the pyranometer. A chassis separate from the SMU chassis was used as a dock for the DAQ. The NI cDAQ 9172 Legacy NI CompactDAQ Chassis was used, as it is capable of measuring a variety of analog and digital signals read from numerous types of data acquisition units. The DAQ along with the chassis are shown in the following two figures, Figure 5.6 and Figure 5.7, respectively.

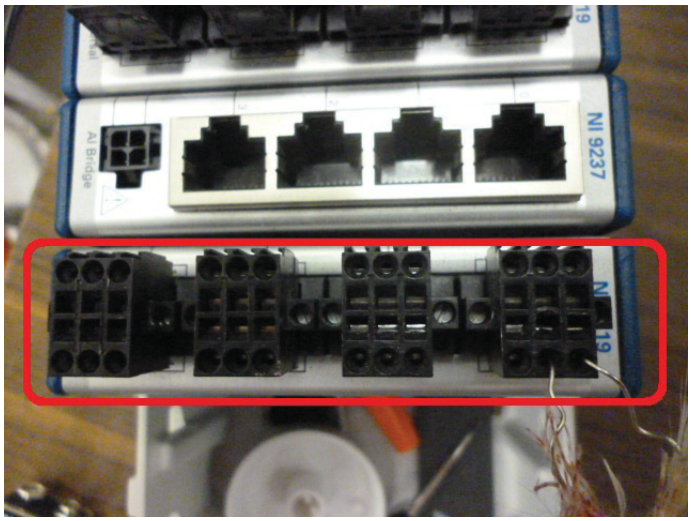

Figure 5.6: NI 9219 DAQ

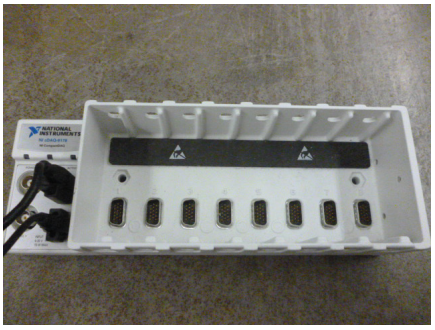

Figure 5.7: NI cDAQ 9172 Chassis

5.2.5 Source Measurement Unit

In order to perform current/voltage sweeps across the solar panel to determine its efficiency, a PXI Source Measure Unit (SMU) was used. The SMU can measure different voltages at a specific current and vice versa, which is useful in finding the systems characteristic IV curve. This IV curve is important in finding the maximum power generated by the solar cell at different light intensities. The specific SMU used in this experiment was the NI PXI-4130 Power SMU made by National Instruments, which is shown plugged into the SMU Chassis in Figure 5.8.

5.2.6 SMU Chassis

The SMU was plugged into a chassis (NI PXIe-1073 5-Slot 3U PXI Express Chassis with AC plus Integrated MXI-Express Controller), which docks the SMU and allows it to be connected alongside other PXI modules in the chassis' five peripheral slots. The chassis also allows connection to a PCI Express card (NI-8360), which allows a PC to be used as a host controller. The chassis with the SMU inserted into slot 1 is shown in Figure 5.8.

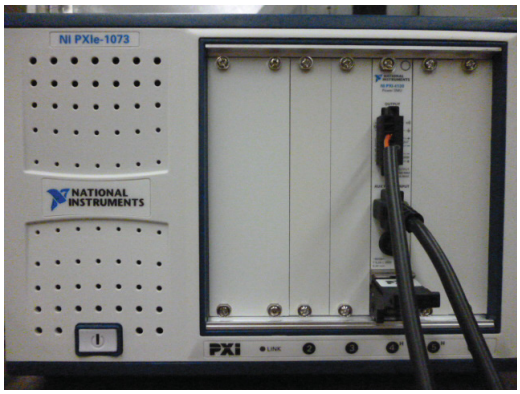

Figure 5.8: NI PXIe-1073 5-Slot 3U PXI Express Chassis

5.2.7 Laptops

Two laptops were used in the experiment. The first laptop, a Dell Vostro, was equipped with Labview 2011. It also contained a slot used for the Express Card which connected to the Power SMU. This laptop was used to control the on/off relay for the lights, as well as measure the temperature, maximum power output, efficiency, etc. The second laptop was a Dell Latitude E5500. A cable attached to the BASIC Stamp Homework Board ran to the laptop. Software for the Homework Board was used to control the rotation of the servo, which varied the dimmer switch to control the irradiance of the light array.

5.2.8 Analog Output Module

The relay required an analog input of 5 Volts to trigger on the lights. The NI 9264 16-Channel Analog Output Module was chosen for this purpose. Each channel consisted of a positive and negative terminal. The wires connected to the relay were connected into the terminals in channel 0. The NI 9264 is shown in Figure 5.9.

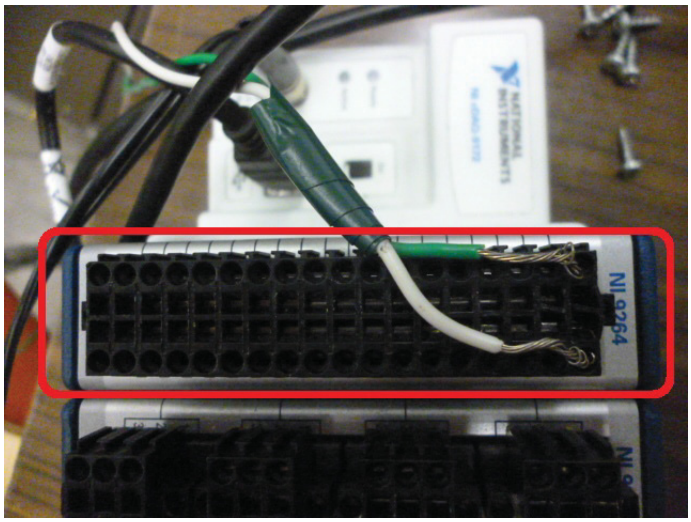

Figure 5.9: NI 9264 Analog Output Module

5.2.9 Light Array Control Board

In order to control various aspects of the lighting, a piece of plywood was cut to be used as a control board. First, a dimmer was installed to change the intensity. It can be very cumbersome to adjust a dimmer by hand and obtain an equal irradiance from a previous experiment, so it was desired to use computer software to control the dimmer. BASIC Stamp was used on a seperate laptop to write a small program which controls a small circuit, called a BASIC Stamp HomeWork Board (manufactured by Paralax). The circuit was specifically wired in a way to control a small servo, also manufactured by Paralax. Plastic gears (gear ratio 1:1) were secured to the tops of the dimmer and servo, which were screwed into the board in a way that would interlock the gears. By changing a number within the BASIC Stamp program and selecting

RUN, the servo (and subsequently the dimmer) was rotated in small increments to achieve a more precise irradiance level in the lights. The BASIC Stamp HomeWork Board (with Duracell Procell 9V alkaline battery) and servo/dimmer switch are shown respectively in Figure 5.10 and Figure 5.11. The BASIC Stamp program is shown in the Appendix.

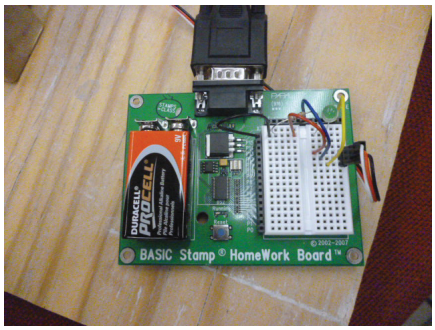

Figure 5.10: Paralax BASIC Stamp HoweWork Board

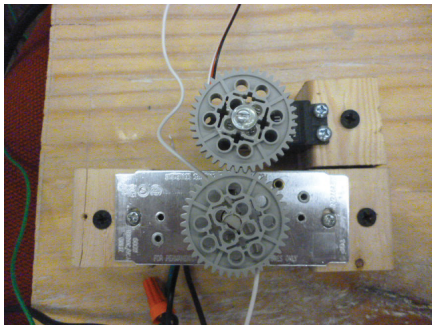

Figure 5.11: Servo Connected to Dimmer Switch

It was desired to create a separate switch for the lights that can be controlled using computer software. A Gold solidstate relay (SAP4825D) was chosen for two purposes: first, it sent a signal to the lights so a button could be pressed in the VI to turn the lights on/off. Secondly, the VI is designed so the user can input a limit temperature. If the thermocouple reads higher than this, the lights would automatically turn off until the temperature fell back below the limit temperature. This protects the solar panel from becoming damaged if the temperature exceeded the factory specified maximum operating temperature of 85 ℃. The relay is shown in figure 5.12.

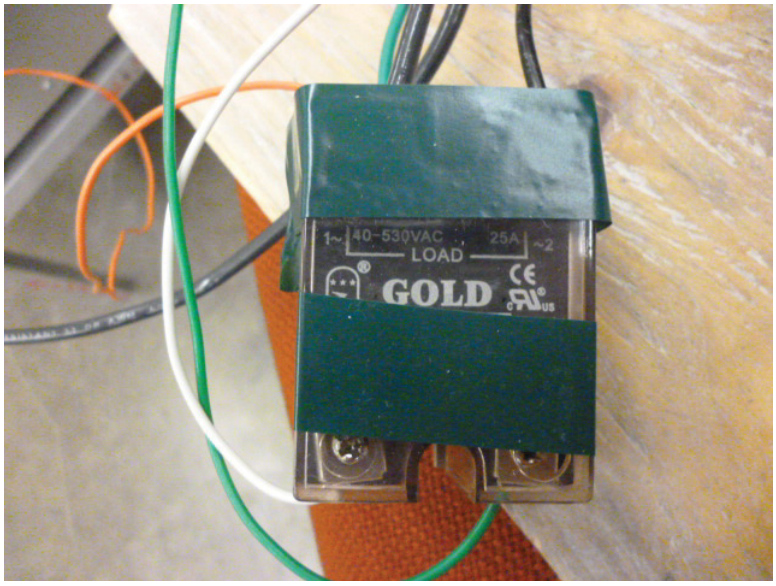

Figure 5.12: Gold Solidstate Relay

5.2.10 Software

The Dell Vostro laptop was installed with Labview 2011 to record the experimental readings from the DAQ and SMU. A Virtual Instrument, VI, is a specific program created within Labview that allows experiments to be recorded through signal manipulation and measurement. The specific VI used in the experiment was obtained from National Instruments' website. This VI allowed the temperature to be recorded. It also displayed pertinent values such as voltage, current, and efficiency. These values were used to show the IV-curve within the VI. Modifications were made, such as converting the temperature to Fahrenheit, adding in a section to control the relay, and allowing the irradiance to be measured and specified prior to taking voltage measurements. A screenshot of the front panel (panel showing graphs and control knobs used for the experiment) as well as a screenshot of the block diagram (which shows the code and wiring that runs in the background of the VI) are shown in Figure 5.13 and Figure 5.14, respectively. Only a small portion of the block diagram is shown. More screenshots of the VI (after obtaining results for the bare panel at different velocities with an irradiance of $1000\frac{W}{m^2}$) are shown in the Appendix.

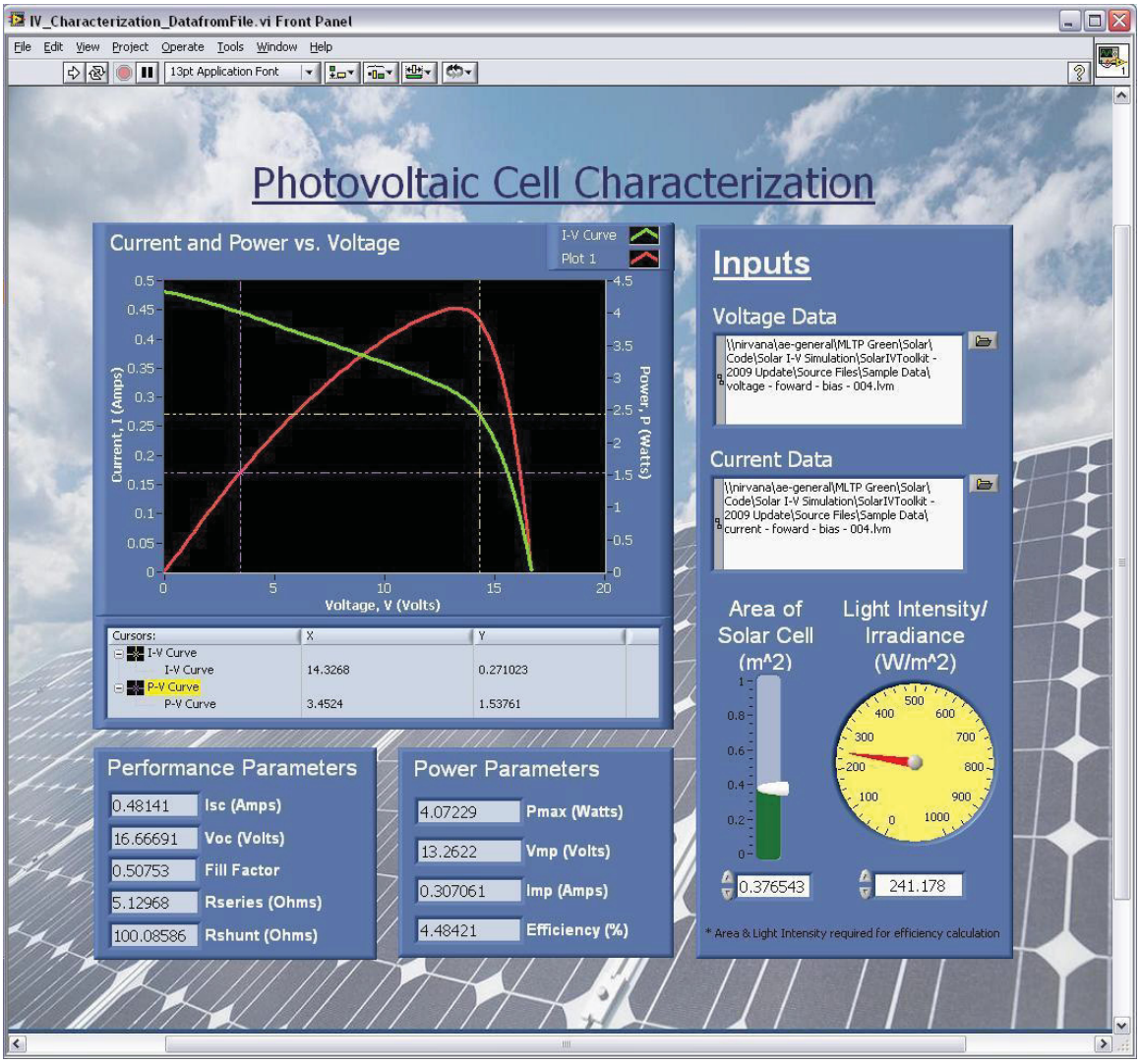

Figure 5.13: Front Panel of VI

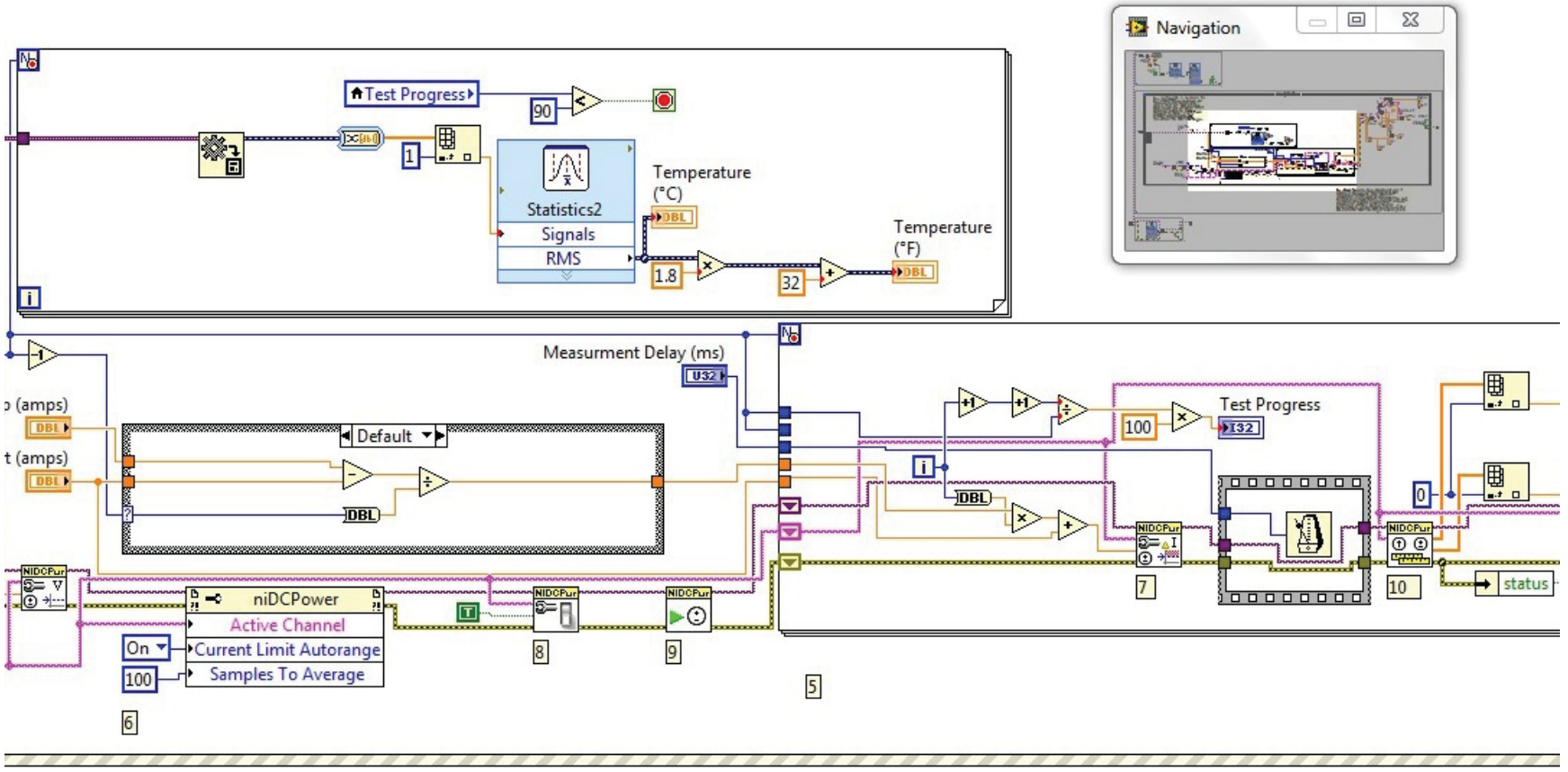

Figure 5.14: Block Diagram of VI

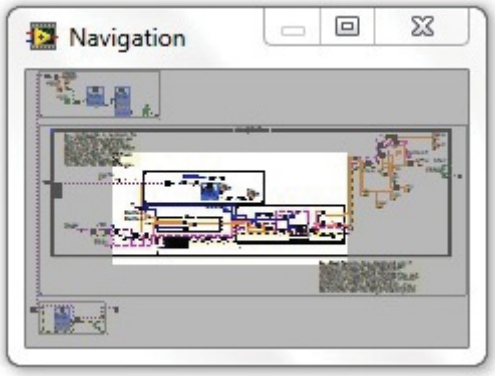

Figure 5.15: Navigation Window

A second, smaller VI was also created in order to measure the irradiance before the experiment was set to start. Once the proper irradiance was achieved, the value was put into the main VI so the calculations for panel efficiency could be calculated correctly. Figure 5.16 shows both the front panel and block diagram of the pyranometer VI.

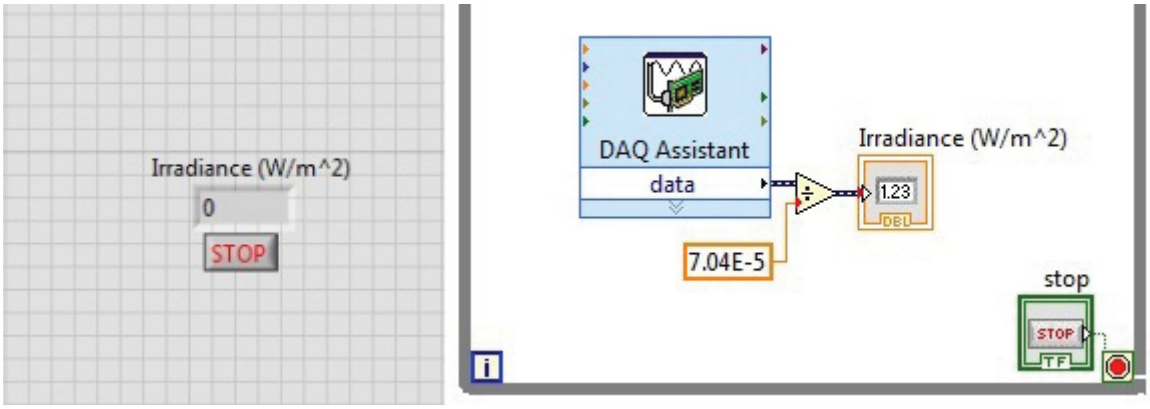

Figure 5.16: Pyranometer VI

5.2.11 Custom Box

A custom-made box was designed in order to mount the solar panel over an array of 90 Watt halogen flood lights. The array consisted of four lights that are wired in parallel to a dimmer switch in order to adjust the light intensity to achieve a proper irradiance. The box itself was constructed by welding together a frame made of aluminum tubing. Flat aluminum panels were screwed to the outside to contain the light. The inner sides of the box were fitted with insulation millboard to minimize loss of heat. The box sat on a seperate frame without aluminum sides so air could flow freely across the backside of the panel. Latches on the box and padding around the edges were used to create a tight fit between the top and bottom sections, to ensure that no light would escape. With the bottom frame detached, the box could be set upside-down in order to provide easier access to the backside of the panel, where various cooling methods were used, such as water film cooling. Figures 5.17, 5.18, and

5.19 show the bottom portion of the box (used as a stand), the top portion of the box (containing the array of halogen lights wired to the dimmer switch and the solar panel) and the fully assembled box, respectively.

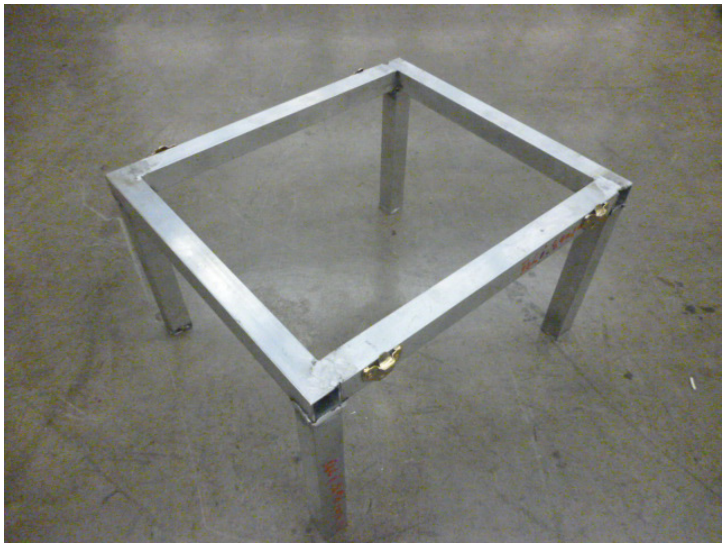

Figure 5.17: Custom Box Stand

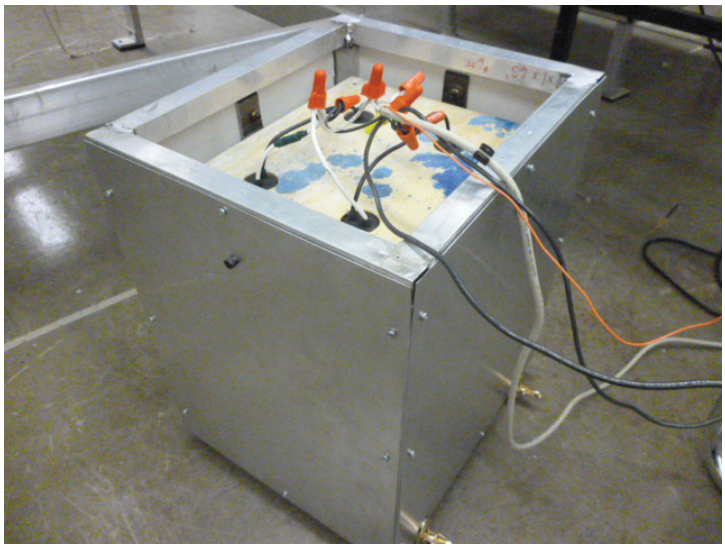

Figure 5.18: Custom Box Top

Figure 5.19: Fully Assembled Box

The array of lights was contained within a piece of plywood, which sat on brackets inside the top portion of the custom box. A seperate piece of plywood was cut with a round hole in the center. This was placed between the two sections of the box (temporarily taking the place of the solar panel). This enabled a pyranometer to be placed in the hole in order to measure the irradiance given off by the lights before the solar panel was placed. Figure 5.20 depicts these two pieces of plywood.

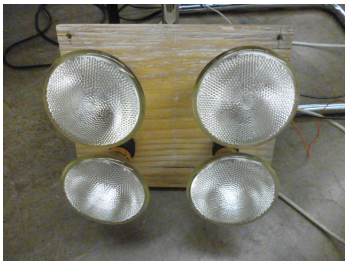

(a) Halogen Flood Lights

(b) Plywood with Measuring Hole

Figure 5.20: Lights and Light Measurement

5.2.12 Ventilation Meter and Fan

A variable speed electric fan (manufactured by Holmes Products Corp.) was used to simulate airflow at different velocities across the backing of the solar panel. The custom box was set at a 10 degree angle and the fan was laid underneath. The velocity was measured using a handheld VelociCalc Plus Multi-Parameter Ventilation Meter 8386. Three different velocities were measured using the device in units of feet per minute. The fan and ventilation meter are shown in Figures 5.21 and 5.22, respectively.

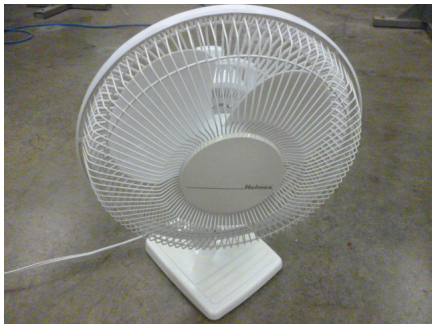

Figure 5.21: Holmes Electric Fan

Figure 5.22: VelociCalc Plus 8386 Ventilation Meter

5.2.13 Fins

Two different fin configurations were chosen for the heat sinks. They were manufactured out of aluminum by Q4 Manufacturing Solutions located in Youngstown, Ohio. Each heat sink consisted of two pieces, which are adhered to the back of their

respective solar panels. This was done using a silicone manufactured by Silicone Solutions. The specific product used was SS-35 Thermally Conductive Silicone RTV. This was chosen for its ability to allow heat flow through the adhesive in order to minimize resistance. It was also chosen for its strength, which allowed the heat sinks to be mounted underneath the solar panel without detaching. The adhesive was made to be highly weather resistant, which is a large factor in solar applications. Figures 5.23 and 5.24 depict the first heat sink with smaller fins and the second heat sink with larger fins and spacing, respectively.

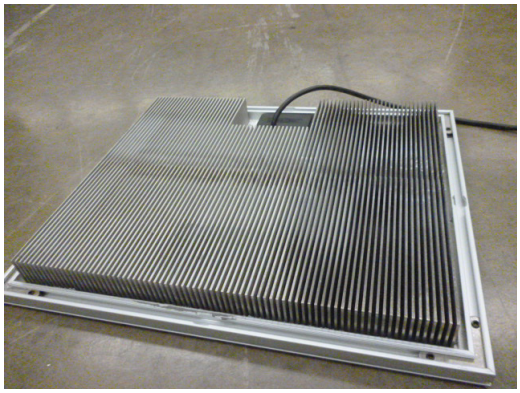

Figure 5.23: Heat Sink 1, Smaller Heat Sink

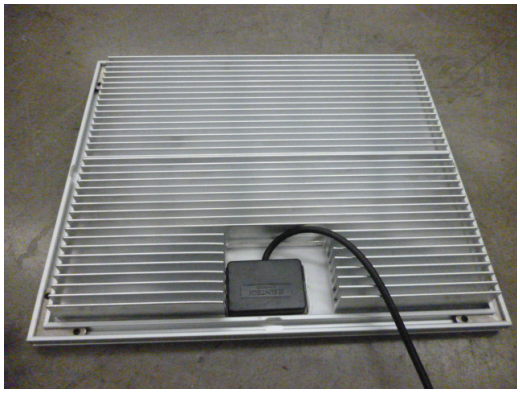

Figure 5.24: Heat Sink 2, Larger Heat Sink

5.3 Method

5.3.1 General Method

The experimental setup started with attaching a thermocouple to the backside of the solar panel using electrical tape. This thermocouple was wired to the DAQ, as well as the wires leading to the relay. A pyranometer was set underneath the reserved piece of plywood, which was placed between the two sections of the box, so the irradiance could be measured at different light intensities. The lead wires from the solar panel were then inserted in the terminals of the SMU. The respective chassis for the SMU and the DAQ were connected to the laptop. The cable running from the BASIC Stamp HomeWork Board was inserted into a terminal in the second laptop. The solar power measurement VI in National Instruments Labview and the BASIC Stamp program were opened on their respective laptops. The VI was then started and the lights were turned on. At this point, it was necessary to allow the lights to sit for a period of time in order for them to heat up and approach steady-state. The radiation indicator attached to the pyranometer was then turned on. Adjustments were made using BASIC Stamp in order to achieve irradiances of approximately $1000\frac{W}{m^2}$, $1250\frac{W}{m^2}$, and $1500\frac{W}{m^2}$, depending on the stage of the experiment. Once the radiation indicator showed a steady irradiance, the experiment was ready to begin.

5.3.2 Phase 1: Bare Panel with Natural Convection

The first phase of experimentation consisted of measuring the efficiency of the bare panel, using no cooling methods (natural convection, which relies solely on the bouyancy of air to naturally create an upward draft). Measurements were taken at the initial temperature, which was at or slightly above room temperature. This involved recording voltage, current, efficiency, and temperature. The panel was then allowed to sit while the solar cells heated up to a steady temperature. Once steady-state

was achieved, a second set of data (also including voltage, current, efficiency, and temperature) was recorded and everything was exported to an Excel spreadsheet. Screenshots were saved for each measurement which shows the IV curves each time a set of data was taken. This experiment was performed three times for the three different chosen irradiances, which gave a total of three sets of data. Figure 5.25 shows the entire experimental setup for Phase 1.

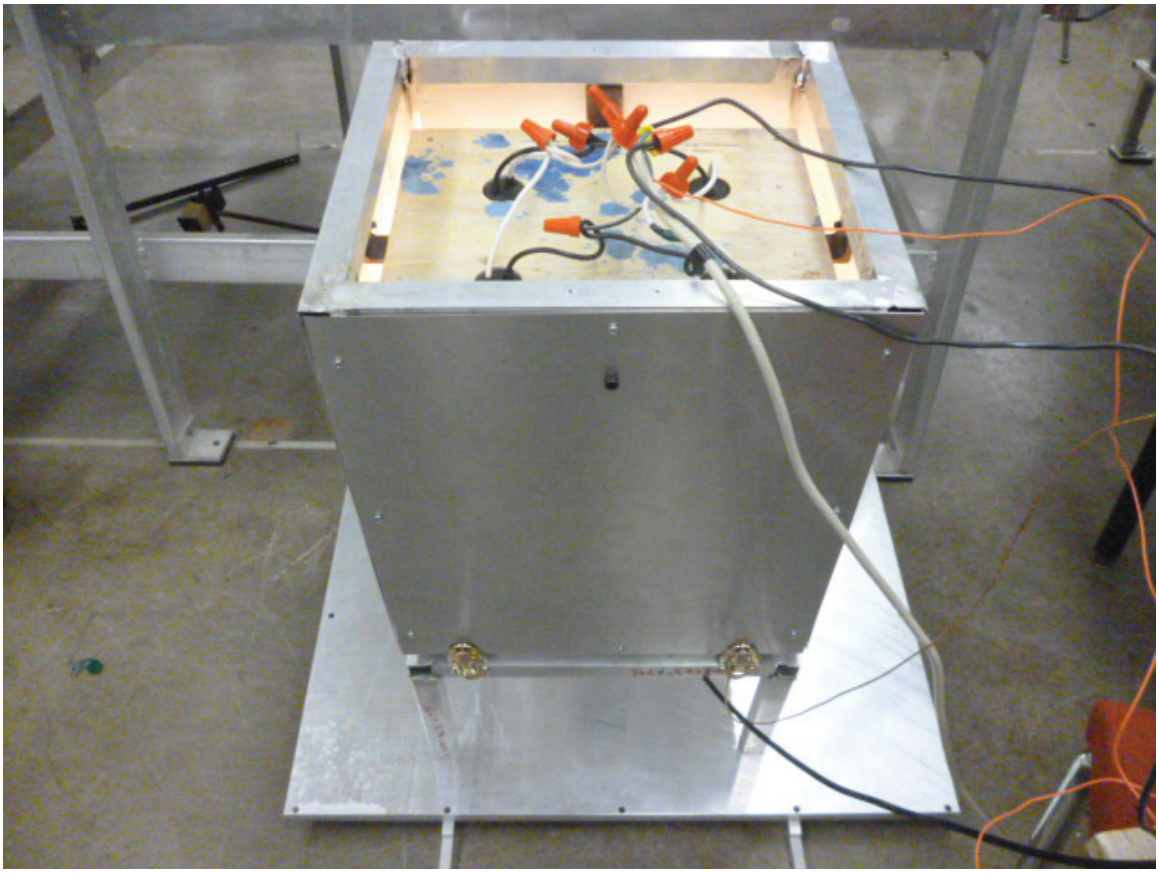

Figure 5.25: Testing Performed with Still Air on Bare Panel

5.3.3 Phase 2: Bare Panel with Forced Convection

It was desired to investigate the temperature at different air velocities. This consisted of starting the experiment identically to Phase 1, with the addition of a fan placed underneath the panel set to its highest setting ($\approx 2.54\frac{m}{s}$). Once the panel

reached a steady temperature, the data was collected and the setting on the fan was changed to medium ($\approx 1.37\frac{m}{s}$). This process was repeated again with the low fan setting ($\approx 1.12\frac{m}{s}$). The experiment was performed three seperate times for the three irradiances. This gave an additional nine sets of data, for a total of twelve sets. The data was tabulated to be compared to the steady-state temperatures for the natural convection experiments. Figure 5.26 shows the experimental setup for this phase.

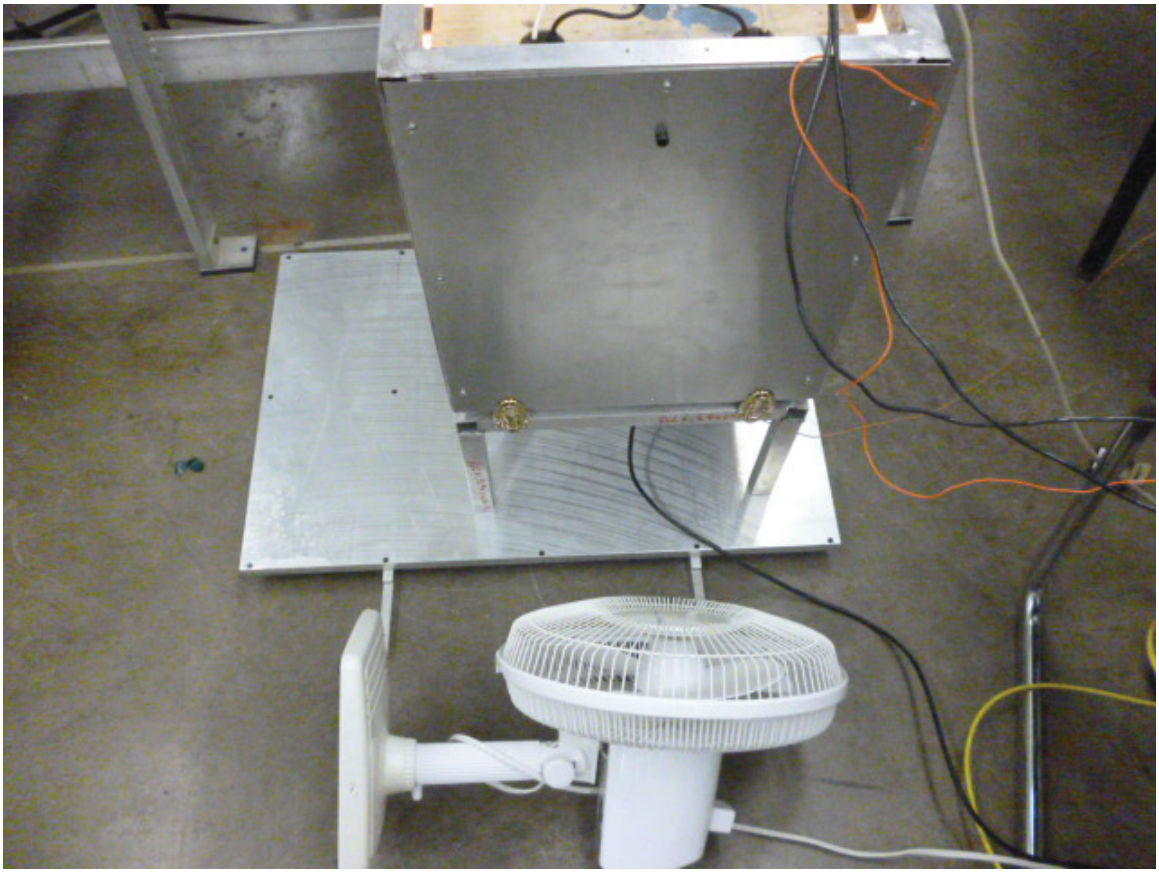

Figure 5.26: Testing Performed with Wind on Bare Panel

5.3.4 Phase 3: Panel with Fins

The third phase was then started with the goal of attaching two fin configurations to the back of their respective solar panels. The heat sinks were attached to the solar panel using a highly conductive thermal adhesive. Thermocouples were attached to

the fins in roughly the center of the solar panel, where the temperature was previously taken without the heat sinks. Since two different heat sinks were manufactured, phases 1 and 2 were repeated for both sets. This gave an additional twleve sets of data for each heat sink, which increased the total number of data sets to 36. The data was once again exported to Excel in order to compare the temperature and efficiency values with the data obtained from the bare panel. This also allowed the data to be compared between the different fin configurations in order to find which design was most effective. Figure 5.27 depicts one of the heat sinks mounted in the box and being measured.

Figure 5.27: Testing Performed on Heat Sink Panel

Chapter 6

Results

There are three different sections to the entire data set. As can be seen in a previous chapter, analytic equations were used to calculate the steady state temperature of the solar panel under idealized conditions. Preliminary analytical results were first found to discover the affects of pin fins and plate fins under different configurations. While the actual analytical results used a heat transfer coefficient calculated using experimental data, the preliminary results were found using a spreadsheet that was set up using arbitrary values for the heat transfer coefficient in order to see the temperature at each value. It was found that plate fins would give a lower temperature at any given heat transfer coefficient for a configuration similar to pin fins (i.e. number of pin fins width-wise equal to number of total plate fins). After this discovery, coupled with the fact that pin fins would be significantly more difficult and expensive to manufacture, led to the decision to only use plate fins in the experimental setup. A small section of this spreadsheet is shown in Figure 6.1, depicting where the geometry could be changed to see how the surface temperature would be affected for different configurations.

		Geometry	
	Panel		Fins
t (m)	4.44E-03	T (m)	0.002
l (m)	0.275	L (m)	0.03
w (m)	0.327	S (m)	0.003
$A_{no\ fin}$ (m^2)	0.089925	# of fins, n	76
L_c (m)	0.074689	A_{fin} (m^2)	1.28
A_{unfin} (m^2)	0.054395	A_c (m^2)	5E-04

Color:	Key:
	Free Choice
	Fixed Value
	Calculated Value
	Reference

Figure 6.1: Section of Master Spreadsheet

6.1 Experimental Results

The experimental data was useful in many ways. On a fundamental level (and most importantly), the data was used to represent real-world results for comparison with an idealized situation predicted by the analytical calculations. The data was then used to compare the many different situations in the experimental setup. For each irradiance tested, and for each individual solar panel, the results could be compared between the different cooling methods. Secondly, the three different solar panels could be compared in identical states. This provided evidence as to which heat sink provided the largest benefit. It also showed how the application of either heat sink would provide a higher amount of cooling for a bare panel under the same conditions. Lastly, the data between each irradiance could be compared. This was done in an attempt to show that the cooling methods should provide the same benefit, independent of the amount of the sun's radiation. While many different values were recorded for each case, tables were made showing only the steady-state temperature, power output at steady-state, and the efficiency of the solar panel. The tables for the three different irradiances of $1000\frac{W}{m^2}$, $1250\frac{W}{m^2}$, and $1500\frac{W}{m^2}$ are shown in Tables 6.1, 6.2, and 6.3, respectively.

Table 6.1: Effect of Temperature on Power Output/Efficiency for Irradiance = $1000\frac{W}{m^2}$

		Wind $\approx$ 2.54 m/s	Wind $\approx$ 1.37 m/s	Wind $\approx$ 1.12 m/s	Wind = 0 m/s
Bare Panel	T_{ss} (℃)	32.0547	33.2057	34.128	60.1916
	P_{ss} (W)	3.31614	3.17732	3.19338	2.81972
	η	4.32844	4.14724	4.1682	3.68048
Sink 1	T_{ss} (℃)	28.7954	29.8608	31.2726	64.4059
	P_{ss} (W)	3.3087	3.33365	3.60498	3.06134
	η	4.31872	4.3513	4.70545	3.99586
Sink 2	T_{ss} (℃)	30.3525	31.242	32.0984	65.5033
	P_{ss} (W)	3.59043	3.64195	3.30321	2.91927
	η	4.68647	4.75371	4.31156	3.81042

Table 6.2: Effect of Temperature on Power Output/Efficiency for Irradiance = $1250\frac{W}{m^2}$

		Wind $\approx$ 2.54 m/s	Wind $\approx$ 1.37 m/s	Wind $\approx$ 1.12 m/s	Wind = 0 m/s
Bare Panel	T_{ss} (℃)	33.3608	34.4098	35.3618	65.9052
	P_{ss} (W)	4.40317	4.37605	4.18621	3.92068
	η	4.59784	4.56952	4.37129	4.09402
Sink 1	T_{ss} (℃)	27.6544	28.9918	30.1841	67.1114
	P_{ss} (W)	4.29869	4.25768	4.35763	3.9708
	η	4.48874	4.44592	4.55029	4.14636
Sink 2	T_{ss} (℃)	30.2154	31.4584	32.5191	68.967
	P_{ss} (W)	3.57338	3.53475	3.86096	3.16149
	η	3.73137	3.69103	4.03166	3.30127

Table 6.3: Effect of Temperature on Power Output/Efficiency for Irradiance = $1500\frac{W}{m^2}$

		Wind $\approx$ 2.54 m/s	Wind $\approx$ 1.37 m/s	Wind $\approx$ 1.12 m/s	Wind = 0 m/s
Bare Panel	T_{ss} (℃)	36.2508	37.3939	37.2835	70.8141
	P_{ss} (W)	5.16061	5.0818	5.11238	4.37274
	η	4.49064	4.42206	4.44868	3.80505
Sink 1	T_{ss} (℃)	29.6765	31.358	32.8838	74.8403
	P_{ss} (W)	5.85221	5.97494	5.92447	5.00712
	η	5.09246	5.19925	5.15533	4.35707
Sink 2	T_{ss} (℃)	34.1372	34.2485	36.0272	76.4637
	P_{ss} (W)	4.98171	5.13099	5.59465	4.40843
	η	4.33497	4.46487	4.86833	3.83612

As discussed previously, there exists a linear correlation between the power output of a solar panel and the surface temperature. Namely, the power output drops over time proportionally to the rise in surface temperature. The experimental results obtained in this thesis showed this to be true. Figure 6.2 shows the temperature data obtained for the bare panel. The rising temperatures in the graph are due to decreases the wind speed. The data is shown for all three irradiances. Equations for the linear relationships for each irradiance are shown next to each trend line. These equations can be used to predict the power output for temperatures outside of the range tested.

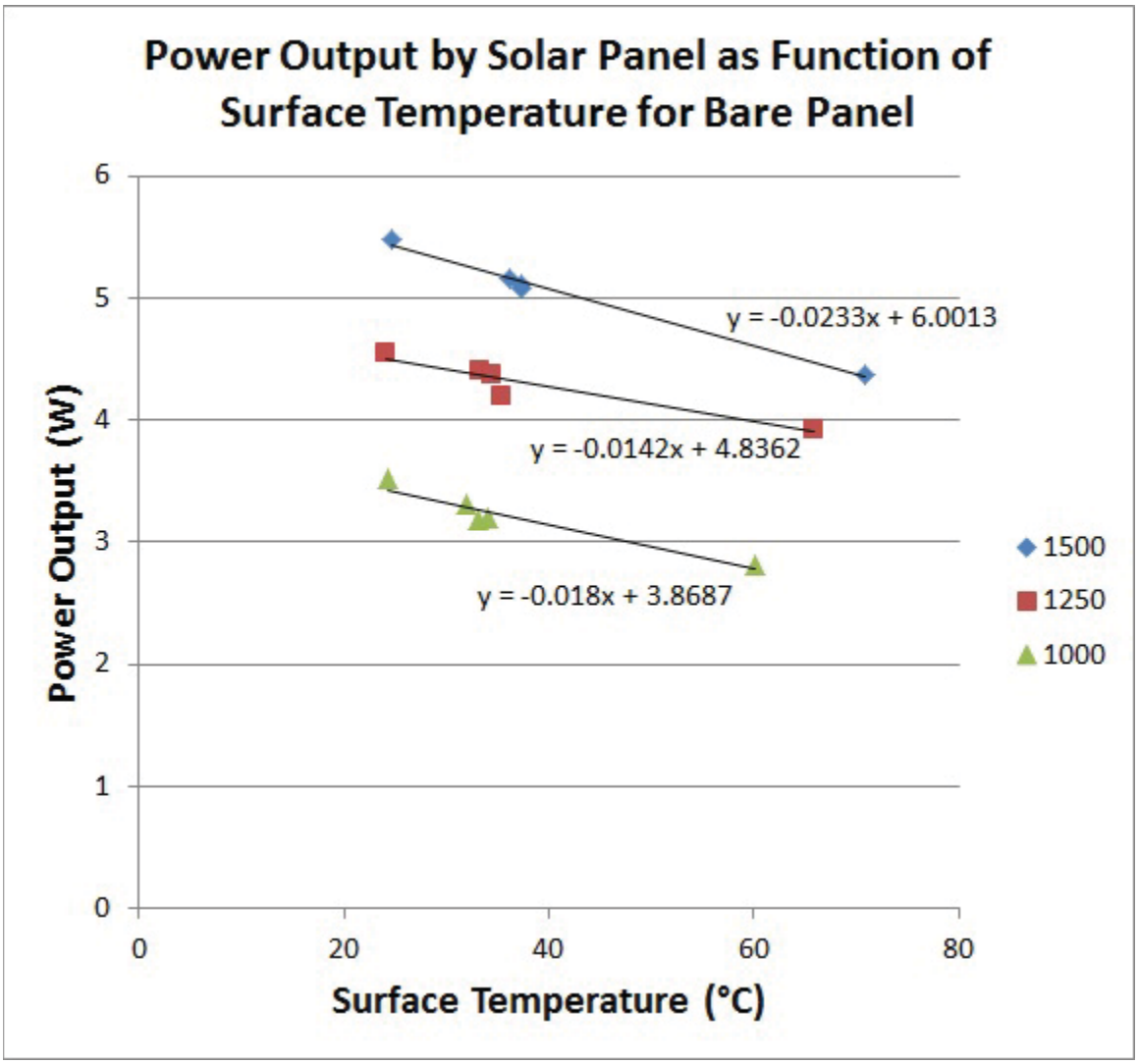

Figure 6.2: Correlation of Power Output and Surface Temperature for Bare Panel

The experimental results were used to find the heat transfer coefficients so they can be used to compare the results to other methods. Tables 6.4, 6.5, 6.6, and 6.7 show the film temperature, Nusselt number, and heat transfer coefficients for each of these cases. To see how the calculations were performed, refer to Subsections 3.5.1, 3.5.2, 3.5.3, and 3.5.4, respectively.

Table 6.4: Heat Transfer Coefficients for Bare Panel, Forced Convection

I $\left(\frac{W}{m^2}\right)$	V (m/s)	T_s (℃)	T_f (℃)	Nu_x	h $\left(\frac{W}{m^2 \cdot K}\right)$
1000	2.54	32.0547	27.02735	86.39	15.87
1000	1.32	33.2057	27.60285	62.17	11.44
1000	1.12	34.128	28.064	57.19	10.54
1250	2.54	33.3608	27.6804	86.22	15.87
1250	1.32	34.4098	28.2049	62.06	11.44
1250	1.12	35.3618	28.6809	57.08	10.53
1500	2.54	36.2508	29.1254	85.84	15.86
1500	1.32	37.3939	29.69695	61.78	11.43
1500	1.12	37.2835	29.64175	56.91	10.53

Table 6.5: Heat Transfer Coefficients for Bare Panel, Natural Convection

I $\left(\frac{W}{m^2}\right)$	T_s (℃)	T_f (℃)	Nu_x	h $\left(\frac{W}{m^2 \cdot K}\right)$
1000	60.1916	41.0958	9.86	3.50
1250	65.9052	43.9526	10.11	3.59
1500	70.8141	46.40705	9.49	3.37

Table 6.6: Heat Transfer Coefficients for Heat Sink Panels, Forced Convection

Heat Sink	I $\left(\frac{W}{m^2}\right)$	V (m/s)	T_s (℃)	T_f (℃)	Nu_x	h $\left(\frac{W}{m^2 \cdot K}\right)$
1	1000	2.54	28.7954	25.3977	0.81	10.39
1	1000	1.32	29.8608	25.9304	0.43	5.55
1	1000	1.12	31.2726	26.6363	0.37	4.71
1	1250	2.54	27.6544	24.8272	0.82	10.41
1	1250	1.32	28.9918	25.4959	0.44	5.56
1	1250	1.12	30.1841	26.09205	0.37	4.72
1	1500	2.54	29.6765	25.83825	0.81	10.38
1	1500	1.32	31.358	26.679	0.43	5.54
1	1500	1.12	32.8838	27.4419	0.37	4.70
2	1000	2.54	30.3525	26.17625	3.24	13.83
2	1000	1.32	31.242	26.621	2.31	9.85
2	1000	1.12	32.0984	27.0492	2.08	8.91
2	1250	2.54	30.2154	26.1077	3.24	13.83
2	1250	1.32	31.4584	26.7292	2.30	9.85
2	1250	1.12	32.5191	27.25955	2.08	8.90
2	1500	2.54	34.1372	28.0686	3.22	13.83
2	1500	1.32	34.2485	28.12425	2.29	9.84
2	1500	1.12	36.0272	29.0136	2.07	8.89

Table 6.7: Heat Transfer Coefficients for Heat Sink Panels, Natural Convection

Heat Sink	I $\left(\frac{W}{m^2}\right)$	T_s (℃)	T_f (℃)	Nu_x	h $\left(\frac{W}{m^2 \cdot K}\right)$
1	1000	64.4059	43.20295	14.64	5.20
1	1250	67.1114	44.5557	10.16	3.60
1	1500	74.8403	48.42015	7.24	2.57
2	1000	65.5033	43.75165	10.09	3.58
2	1250	68.967	45.4835	10.23	3.63
2	1500	76.4637	49.23185	10.47	3.72

6.1.1 Fin Performance

The results showed that the heat sink panels performed better than the bare panel (with forced convection), as can be seen with the lower steady state temperatures. For natural convection, the heat sink panels actually performed worse, with a higher steady state temperature than the bare panel. Heat sink 1 can also be shown to perform slightly better than heat sink 2. However, the benefits of heat sink 1 over heat sink 2 for all tests and the benefits of the heat sinks versus the bare panel for forced convection were small. This leads to the conclusion that the added benefit is insignificant considering the high cost of manufacturing the heat sinks. Figure 6.3 shows a graph which compares the performance for the two heat sink panels and the bare panel for an irradiance of $I = 1000\frac{W}{m^2}$.

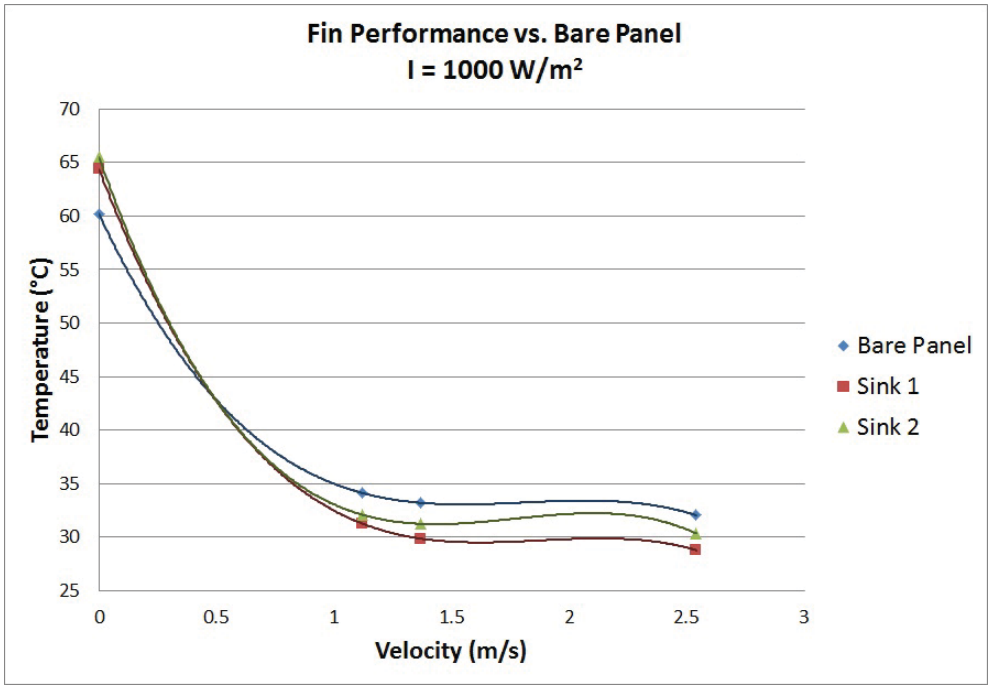

Figure 6.3: Graph Comparing the Performance of the Heat Sink Panels vs. Bare Panel at Each Velocity for $I = 1000\frac{W}{m^2}$

6.2 Analytical Comparison

Due to the complexity of the calculations, analytical results were found for only the case of natural convection with the bare panel. The temperatures for each irradiance in this case are shown in Table 6.8, in comparison with the computational and experimental results for the same case. Also shown are the percent differences between analytical/computational and analytical/experimental. As can be seen, the percentage difference is extremely small between the analytical and computational results. The experimental results, however, deviated significantly from the other two methods. Refer to Figure 6.4 for a graph comparing the three methods.

Table 6.8: Comparison of Results for Bare Panel, Natural Convection

I ($\frac{W}{m^2}$)	T_{anal} (℃)	T_{comp} (℃)	% Diff Anal. Vs. Comp.	T_{exp} (℃)	% Diff Anal. Vs. Exp.
1000	165.66324	166.8	0.68	60.1916	93.40
1250	199.29633	200.71	0.71	65.9052	100.60
1500	241.76036	243.46	0.70	70.8141	109.38

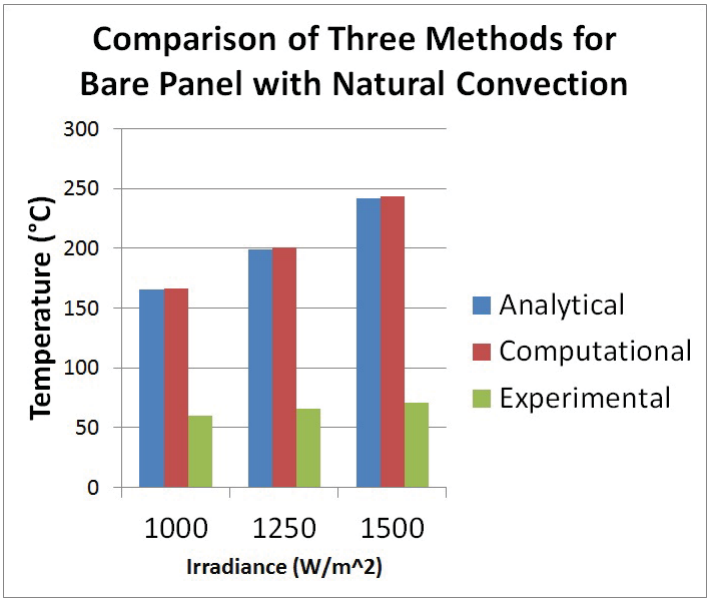

Figure 6.4: Clustered Column Graph Comparing the Results from Three Methods for the Bare Panel with Natural Convection

6.3 Computational Results Vs. Experimental

The experimental and computational calculations were performed for each case. This includes the temperatures for each speed at the three irradiances, for the bare panel and both heat sinks. Tables 6.9, 6.10, and 6.11 show the temperatures compared for computational and experimental for the bare panel, sink 1, and sink 2, respectively.

Table 6.9: Comparison of Computational and Experimental Results For Bare Panel

Bare	$1000\frac{W}{m^2}$		$1250\frac{W}{m^2}$		$1500\frac{W}{m^2}$	
	Comp.	Exp.	Comp.	Exp.	Comp.	Exp.
0 m/s	166.800 ℃	60.1916 ℃	200.710 ℃	65.9052 ℃	243.460 ℃	70.8141 ℃
1.12 m/s	139.689 ℃	34.128 ℃	167.478 ℃	35.3618 ℃	196.076 ℃	37.2835 ℃
1.37 m/s	126.758 ℃	33.2057 ℃	152.176 ℃	34.4098 ℃	179.541 ℃	37.3939 ℃
2.54 m/s	102.735 ℃	32.0547 ℃	122.512 ℃	33.3608 ℃	140.830 ℃	36.2508 ℃

Table 6.10: Comparison of Computational and Experimental Results For Sink 1

Sink 1	$1000\frac{W}{m^2}$		$1250\frac{W}{m^2}$		$1500\frac{W}{m^2}$	
	Comp.	Exp.	Comp.	Exp.	Comp.	Exp.
0 m/s	130.720 ℃	64.4059 ℃	144.920 ℃	67.1114 ℃	177.167 ℃	74.8403 ℃
1.12 m/s	49.519 ℃	31.2726 ℃	55.640 ℃	30.1841 ℃	61.779 ℃	32.8838 ℃
1.37 m/s	45.977 ℃	29.8608 ℃	51.216 ℃	28.9918 ℃	56.342 ℃	31.358 ℃
2.54 m/s	36.793 ℃	28.7954 ℃	39.518 ℃	27.6544 ℃	42.225 ℃	29.6765 ℃

Table 6.11: Comparison of Computational and Experimental Results For Sink 2

Sink 2	$1000\frac{W}{m^2}$		$1250\frac{W}{m^2}$		$1500\frac{W}{m^2}$	
	Comp.	Exp.	Comp.	Exp.	Comp.	Exp.
0 m/s	112.244 ℃	65.5033 ℃	125.283 ℃	68.967 ℃	137.343 ℃	76.4637 ℃
1.12 m/s	46.138 ℃	32.0984 ℃	51.220 ℃	32.5191 ℃	56.141 ℃	36.0272 ℃
1.37 m/s	42.997 ℃	31.242 ℃	47.923 ℃	31.4584 ℃	52.409 ℃	34.2485 ℃
2.54 m/s	37.937 ℃	30.3525 ℃	40.784 ℃	30.2154 ℃	43.771 ℃	34.1372 ℃

6.4 Explanation of Results

As can be seen in the comparison tables, the computational and analytical results matched for the cases that the analytical results were found. However, the experimental results were in disagreement with the computational and analytical results. There

are many reasons why the experimental results are significantly lower. Since the light intensity was adjusted with a dimmer in order to measure the temperature at the proper irradiance values (1000, 1250, and 1500 $\frac{W}{m^2}$), it is likely that the irradiance measured using the pyranometer was higher than the radiation actually generated by the lights. The lights were in very close proximity to the solar panels/pyranometer. This causes the irradiance to vary widely as the pyranometer is moved into different positions around the panel. The maximum value could be seen to be directly underneath one of the light bulbs. As the pyranometer is moved, this irradiance value was shown to drop. A few readings were taken around the panel using the pyranometer after the initinal experiments, and an average was taken to get a better idea of the irradiance instead of the maximum value. However, it would have been more accurate to integrate the light intensity across the entire area of the panel. It can be shown that lowering the irradiance values by a specific factor in the analytical and computational calculations causes the temperatures to match up with the experimental data. Table 6.12 shows the results in ANSYS when the irradiance values were decreased by a factor of approximately 4.5. The data is for sink 1, with an air velocity of $2.54\frac{m}{s}$. The factor by which the irradiance was decreased was adjusted until the temperatures approached the temperatures found in the experiment, until a factor of 4.5 was found to be the closest fit.

Table 6.12: Experimental Results Compared to Computational Results When Irradiance Decreased in ANSYS

$I(\frac{W}{m^2})$	T_{exp} (℃)	$T_{comp,adjusted}$ (℃)
1000 - 222	28.7954	28.234
1250 - 277.5	27.6544	28.808
1500 - 333	29.6765	29.393

In the future, steps can be taken to avoid measuring an exaggerated irradiance. A simple fix would be to use a light setup that is further away from the panels. This would cause the light intensity (and irradiance) to be more uniform across the solar

panel so it could be measured at a single point without worrying about variance as the pyranometer is moved around. Also, it would be helpful to measure the irradiance at as many spots as possible in order to calculate a more accurate average. Calculations would also be made that would integrate the irradiance across the panel. The panel also might not have had optimal thermal properties. The ARC layer (Anti-Reflective Coating) may have not been applied properly to the panel. This would cause a large amount of the radition to be reflected instead of absorbed, which would signinifantly lower the maximum temperatures of the panel when it reaches steady-state.

Chapter 7

Proposed Cooling Method

The data showed no significant benefit in using a heat sink versus a bare panel, as the increase in efficiency was minimal. As an alternative, another cooling method was conceived. This would use a pump to send coolant into channels attached to the back of an array of solar panels (an array should be used, as the larger the array, the bigger the ratio between power saved to power used by a pump). The coolant would pump into a reservoir, where it would be dispersed to each channel that runs down the length of the array backing. At the bottom, the coolant would collect into another reservoir and be pumped into a cooling device to remove heat so it can repeat the cycle. A schematic showing the setup is shown in Figure 7.1.

Ideally, the solar panel would operate at a constant temperature close to the ambient temperature. The tubes running along the back side can be assumed to have the same wall (surface) temperature as the solar panel backing. The temperature of the fluid would approach the panel temperature asymptotically as it travels through the channels across the panel backing. Figure 7.2 is a diagram showing this relationship. Note the rate of exponential decay of the temperature difference between the fluid and surface in the direction of flow.

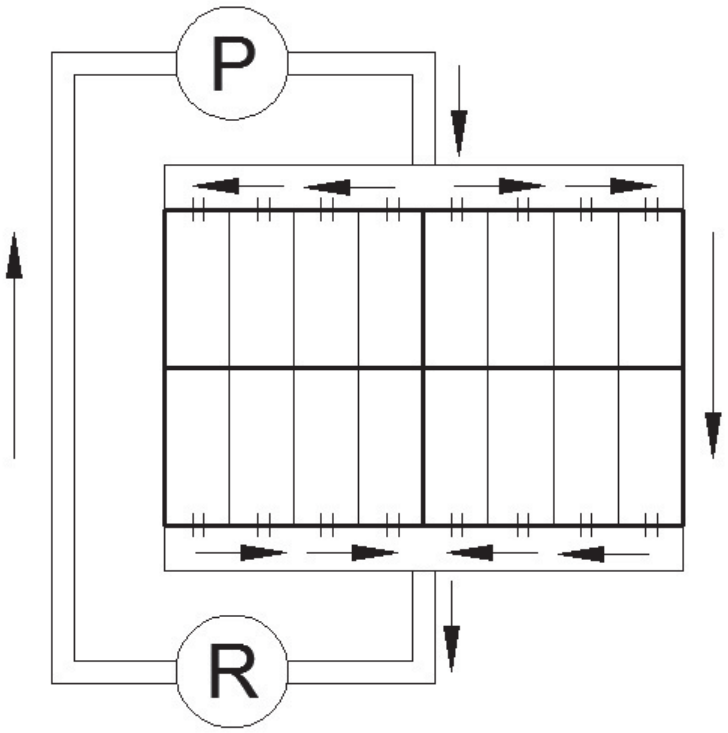

Figure 7.1: Pump Cooling Schematic

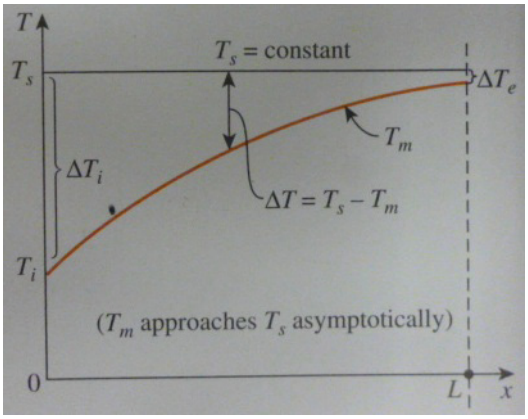

Figure 7.2: Fluid Temperature

If it was desired to design the channels so that the length enables the cooling fluid to heat to a temperature within a degree or two of the constant cell temperature (which assures that the coolant is removing as much heat as possible), the surface temperature can be calculated. This would give an idea of the amount of heat that should be removed from the coolant once the heated cooling fluid passes through a

cooling device. This calculation involves finding the log mean temperature difference between the inlet and outlet temperatures of the coolant as they compare to the surface temperature. First, values for T_i and T_e should be chosen. The value for T_i should be chosen to be relatively low, and the value for T_e should be close to the ambient temperature (or the target temperature for the surface). The number of transfer units (NTU, see equation below) should be adjusted until the surface temperature is calculated to be within a degree or two of the exit temperature. The NTU of the fluid is a dimensionless value that represents how effective the heat transfer system is [Çengel and Ghajar, 2011]. As the NTU approaches a value of 2, the temperature of the surface should be very close to the exit temperature [Çengel and Ghajar, 2011]. The NTU depends on the surface area, mass flow rate of the fluid, constant average convection heat transfer coefficient, and the specific heat capacity ($NTU = \frac{hA_s}{\dot{m}c_p}$). This calculation is performed as follows:

$$T_s = \frac{T_e e^{NTU} - T_i}{e^{NTU} - 1} \tag{7.1}$$

In the next step, the mass flow rate should be calculated using the chosen value for NTU. This will allow the proper size pump to be chosen. Note that in this step, the mass flow rate may require the use of a pump that needs more power than desired. If this is the case, the calculations can be started over and iterations performed in order to find the balance that suits the design requirements. This equation is derived from rearranging the NTU equation and solving for mass flow rate.

$$\dot{m} = \left(\frac{hA_s}{c_p}\right) NTU \tag{7.2}$$

The last step involves calculating the heat transfer rate. This allows the size of the cooling device to be chosen, as it is known how much heat it must draw from the heated coolant. This calculation makes use of the log mean temperature difference (LMTD).

The equations for LMTD and the heat transfer rate are shown below, respectively.

$$\Delta T_{lm} = \frac{\Delta T_e - \Delta T_i}{ln\frac{\Delta T_e}{\Delta T_i}} \tag{7.3}$$

$$\dot{Q} = hA_s\Delta T_{lm} \tag{7.4}$$

Chapter 8

Conclusion

In conclusion, the experiments proved that the heat sinks do indeed have a lowering effect on the solar panel temperature. Sink 1 was shown to perform slightly better than Sink 2. However, each sink only performed slightly better than the bare panel at wind speeds greater than zero. With stagnant air, the heat sinks actually performed worse as they began acting like an insulator. Even with constant wind, it would not be economically feasible to purchase a machined aluminum heat sink if the benefit is as small as the experiments showed. Therefore, it is best to go with the previously mentioned cooling method using water and a pump.

The price of a pump would be significantly cheaper than purchasing an aluminum heat sink. The energy needed to power the pump would be minimal. Some of the energy saved from keeping the solar panel cooler could actually be used to power the pump. This would negate the need for an external power supply, thus simplifying the entire system. Perhaps the largest benefit would arise from the system's ability to be adjusted in order to keep the solar panel surface as cool as desired. However, more research and experimental work must be done in the pump cooling method in order to solidify the analytical findings.

Bibliography

[1] "Agua Caliente Solar Project." *First Solar*. N.p., n.d. Web. 22 Apr. 2013. <http://www.firstsolar.com/en/Projects/Agua-Caliente-Solar-Project>.

[2] AL-Sabounchi, A.M. "Effect of Ambient Temperature on the Demanded Energy of Solar Cells at Different Inclinations." *Renewable Energy* 14 (1998): 149-55. *Academic Search Complete*. Web. 2 Aug. 2011.

[3] "ANSYS Fluent." *ANSYS*. ANSYS, Inc. Web. 4 Sept. 2013.

[4] "ANSYS Mechanical." *ANSYS*. ANSYS, Inc. Web. 11 July 2011.

[5] Bergman, Theodore L., Adrienne S. Lavine, Frank P. Incropera, and David P. Dewitt. *Fundamentals of Heat and Mass Transfer*. 7th ed. Hoboken, NJ: John Wiley & Sons, 2011. Print.

[6] Çengel, Yunus A., and Afshin J. Ghajar. *Heat and Mass Transfer: Fundamentals & Applications*. 4th ed. New York: McGraw-Hill, 2011. Print.

[7] "Climate Data Summary." *Western Regional Climate Center*. Desert Research Institute. Web. 11 July 2011. <http://www.wrcc.dri.edu/cgi-bin/clilcd.pl?az23183>.

[8] Desilvestro, Hans. "What Physical Factors Affect Current-Voltage Characteristics of Dye Solar Cells?" *Dysol*. Feb. 2008. Web. 19 Mar. 2012.

[9] Duffie, John A., and William A. Beckman. *Solar Engineering of Thermal Processes*. 3rd ed. Hoboken, NJ: Wiley, 2006. Print.

[10] Ferguson, L. G., and L. M. Fraas. "Theoretical Study of GaSb PV Cell Efficiency as a Function of Temperature." *Solar Energy Materials and Solar Cells* 39 (1995): 11-18. *ScienceDirect*. Web. 2 Aug. 2011.

[11] Fukushige, Shunichi, Kyoko Ichida, Takashi Minemoto, and Hideyuki Takakura. "Analysis of the Temperature History of Amorphous Silicon Photovoltaic Module Outdoors." *Solar Energy Materials & Solar Cells* 93.6-7 (2009): 926-31. *OhioLINK Electronic Journal Center*. Web. 14 June 2011.

[12] *How Photovoltaic Solar Cells Work*. Digital image. *Total*. N.p., n.d. Web. 22 Apr. 2013. <http://www.total.com/en/our-energies/alternative-energy/solar-energy/background/photovoltaic-922683.html>.

[13] Ishibashi, Ken-ichi, Yasuo Kimura, and Michio Niwano. "An Extensively Valid and Stable Method for Derivation of All Parameters of a Solar Cell from a Single Current-voltage Characteristic." *Journal of Applied Physics* 103 (2008): 094507-1-94507-5. *Academic Search Complete*. Web. 19 Mar. 2012.

[14] Joshi, Anand S., and Arvind Tiwari. "Energy and Exergy Efficiencies of a Hybrid Photovoltaic-thermal (PV/T) Air Collector." *Renewable Energy* 32 (2007): 2223-241. *Academic Search Complete*. Web. 20 June 2011.

[15] Lee, B., J. Z. Liu, B. Sun, C. Y. Shen, and G. C. Dai. "Thermally Conductive and Electrically Insulating EVA Composite Encapsulants for Solar Photovoltaic (PV) Cell." *EXPRESS Polymer Letters* 2.5 (2008): 357-63. *Academic Search Complete*. Web. 15 June 2011.

[16] McQuiston, Faye C., Jerald D. Parker, and Jeffrey D. Spitler. *Heating, Ventilating, and Air Conditioning: Analysis and Design*. 6th ed. Hoboken, NJ: John Wiley & Sons, 2005. Print.

[17] Mossayebi, Faramarz. "Finite Element Analysis of Heat Conduction in the Absorber Plate of a Solar Collector." Thesis. Youngstown State University, 1987. Print.

[18] Nishioka, L., T. Hatayama, Y. Uraoka, T. Fuyuki, R. Hagihara, and M. Watanabe. "Field-test Analysis of PV System Output Characteristics Focusing on Module Temperature." Solar Energy Materials & Solar Cells 75.3/4 (2003): 665-71. Academic Search Complete. Web. 9 Aug. 2011.

[19] Ogueke, N. V., E. E. Anyanwu, and O. V. Ekechukwu. "A Review of Solar Water Heating Systems." *Journal of Renewable and Sustainable Energy* 1.4 (2009): 043106. *Academic Search Complete*. Web. 20 Apr. 2013.

[20] "Part II - Photovoltaic Cell I-V Characterization Theory and LabVIEW Analysis Code." *National Instruments: Test, Measurement, and Embedded Systems*. National Instruments Corporation, 4 Dec. 2009. Web. 3 Jan. 2012.

[21] *A Power Tower Power Plant*. Digital image. *Energy Efficiency and Renewable Energy*. U.S. Department of Energy, n.d. Web. 22 Apr. 2013. <http://www.eere.energy.gov/basics/renewable_energy/power_tower.html>.

[22] Rim, Seung-Bum, Shanbin Zhao, Shawn R. Scully, Michael D. McGehee, and Peter Peumans. "An Effective Light Trapping Configuration for Thin-film Solar Cells." *Applied Physics Letters* 91.243501 (2007). Web. 13 June 2011.

[23] Roberts, Billy. *Photovoltaic Solar Resource of the United States"*. Digital image. *NREL*. National Renewable Energy Laboratory, 20 Oct. 2008. Web. 11 July 2011.

[24] Royne, Anja, and Christopher J. Dey. "Design of a Jet Impingement Cooling Device for Densely Packed PV Cells under High Concentration." *Solar Energy* 81 (2007): 1014-024. *Academic Search Complete*. Web. 10 July 2011.

[25] Shahsavar, A., M. Salmanzadeh, M. Ameri, and P. Talebizadeh. "Energy Saving in Buildings by Using the Exhaust and Ventilation Air for Cooling of Photovoltaic Panels." *Energy and Buildings* 43.9 (2011): 2219-226. *Academic Search Complete*. Web. 20 Apr. 2013.

[26] Skoplaki, E., A. G. Boudouvis, and J. A. Palyvos. "A Simple Correlation for the Operating Temperature of Photovoltaic Modules of Arbitrary Mounting." *Solar Energy Materials & Solar Cells* 92.11 (2008): 1393-402. *OhioLINK Electronic Journal Center*. Web. 14 June 2011.

[27] Solar Thermal Energy. Digital image. *Genesis Energy Solutions*. N.p., n.d. Web. 22 Apr. 2013. <http://genesisenergysolutions.com/energy-solutions/solar-thermal>.

[28] Tayebjee, Murad J. Y., Louise C. Hirst, N. J. Ekins-Daukes, and Timothy W. Schmidt. "The Efficiency Limit of Solar Cells with Molecular Absorbers: A Master Equation Approach." *Journal of Applied Physics* 10.12 (2010): 124506. *Academic Search Complete*. Web. 13 June 2011.

[29] Teertstra, P., M. M. Yovanovich, and J. R. Culham. "Analytical Forced Convection Modeling of Plate Fin Heat Sinks." *Journal of Electronics Manufacturing* 10.4 (2000): 253-61. Web. 22 April 2013.

Appendix A

Screenshots

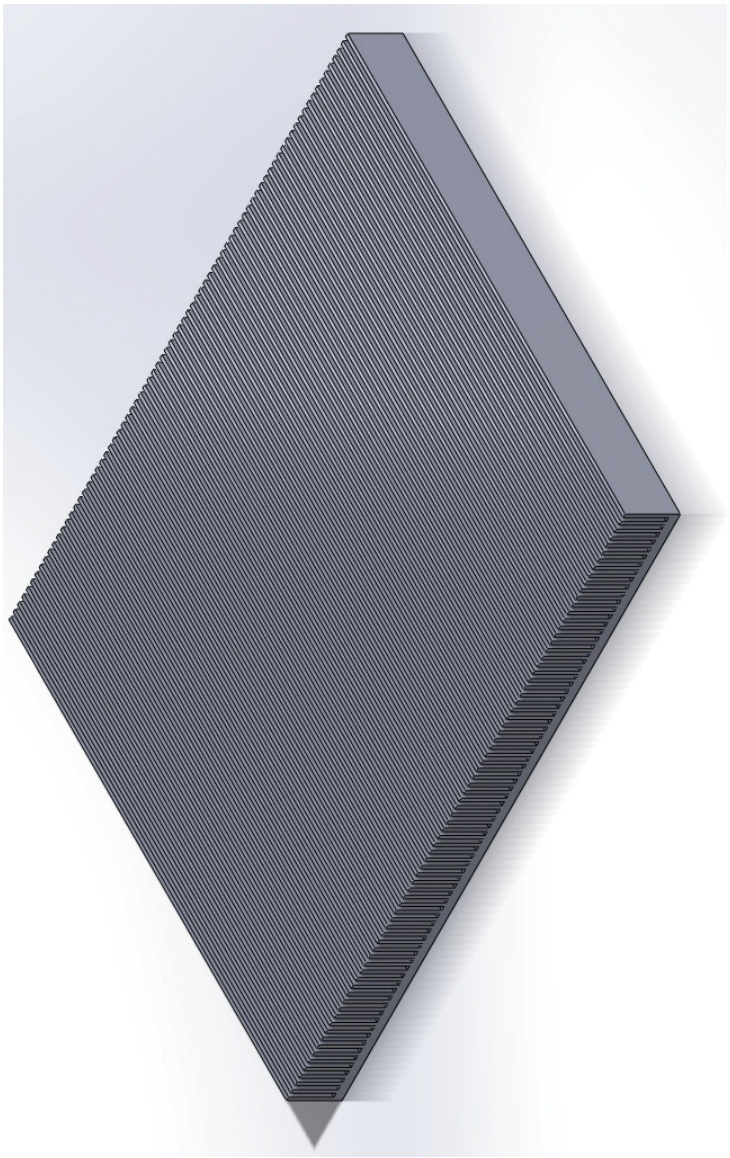

Figure A.1: Isometric of Sink 1 in Solidworks

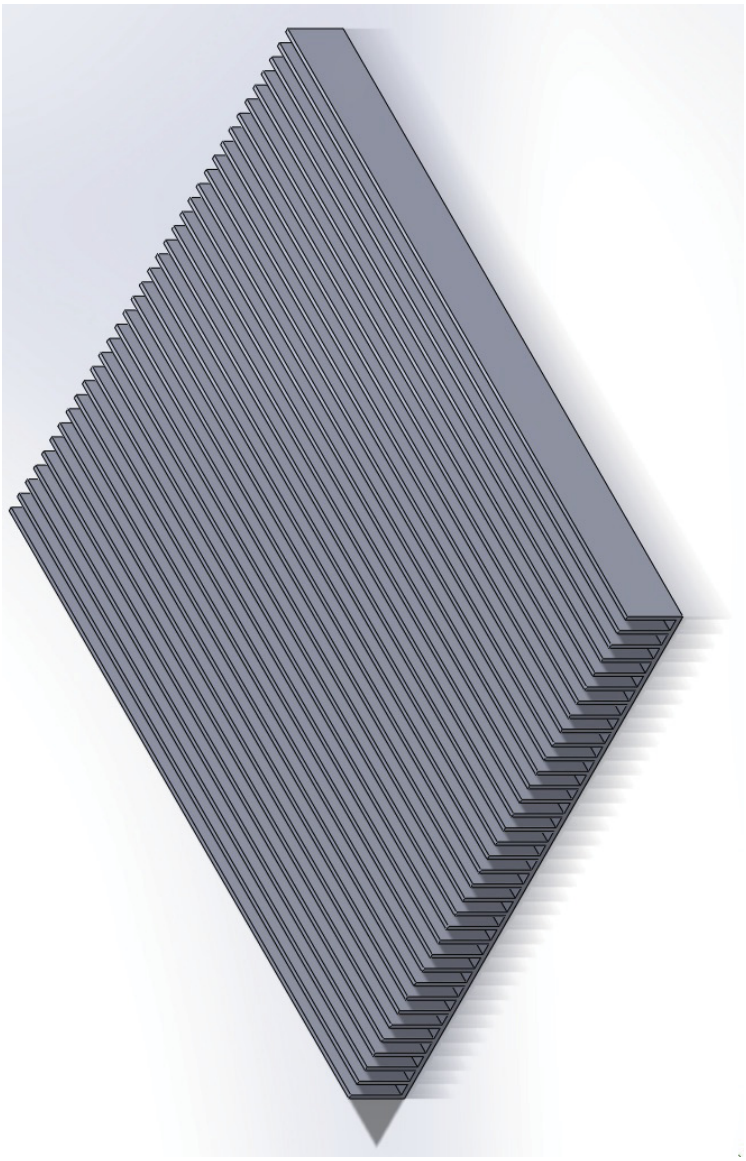

Figure A.2: Isometric of Sink 2 in Solidworks

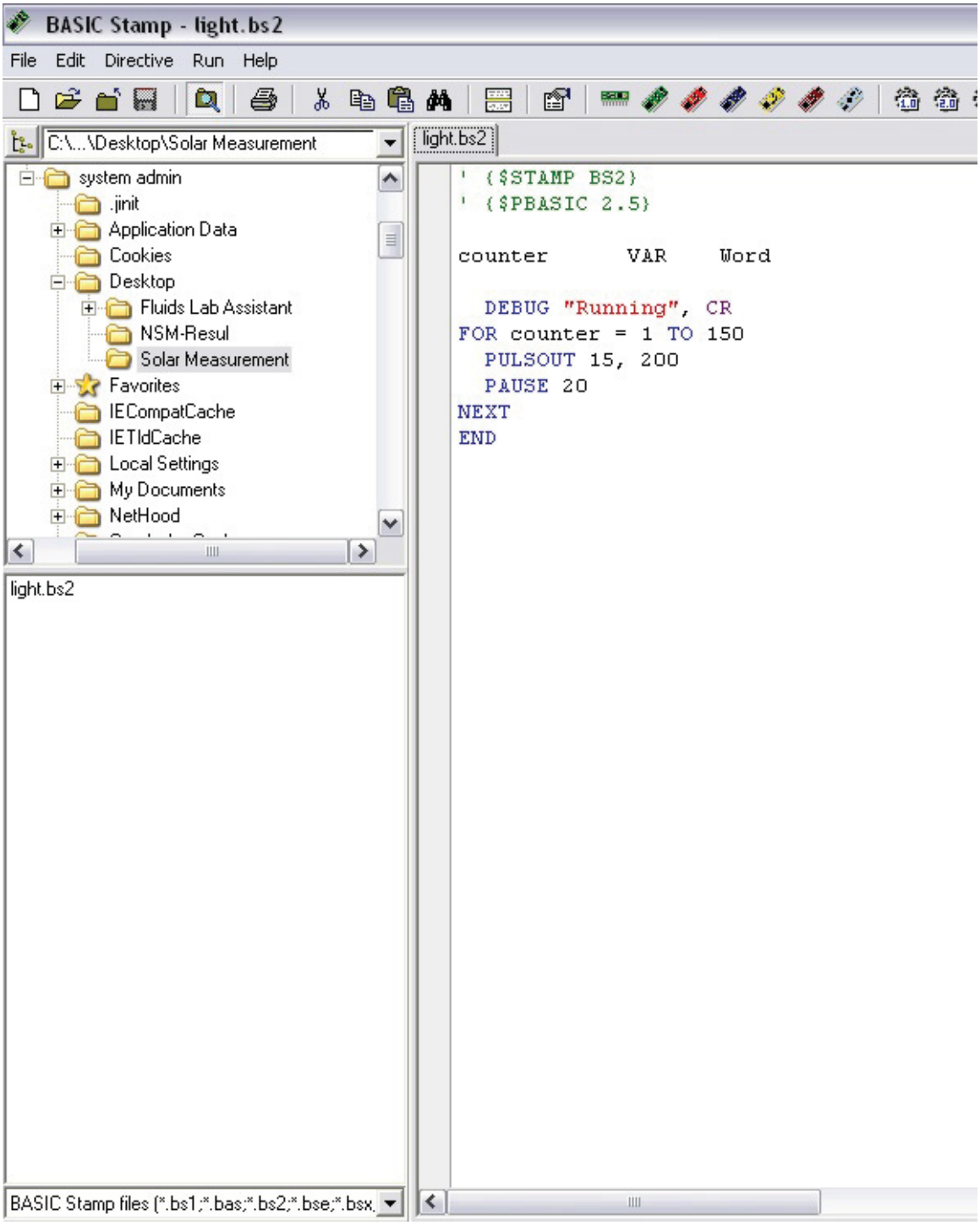

Figure A.3: Light Control Program in BASIC Stamp

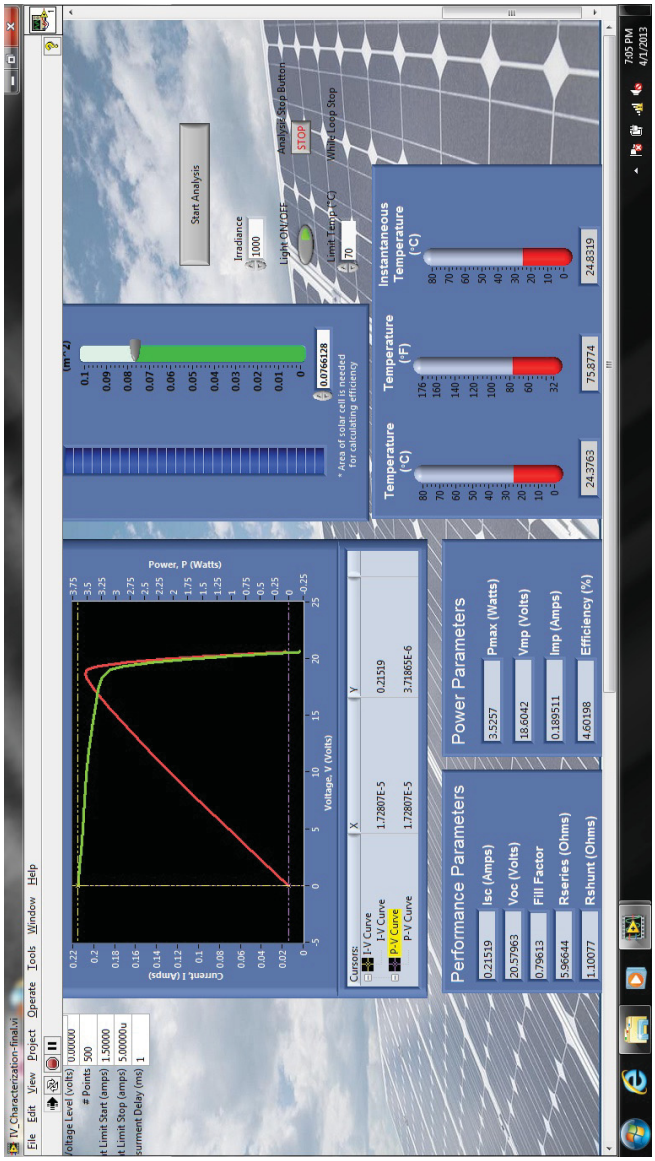

Figure A.4: Bare Panel Starting at Room Temperature, $I = 1000\frac{W}{m^2}, V = 0\frac{m}{s}$

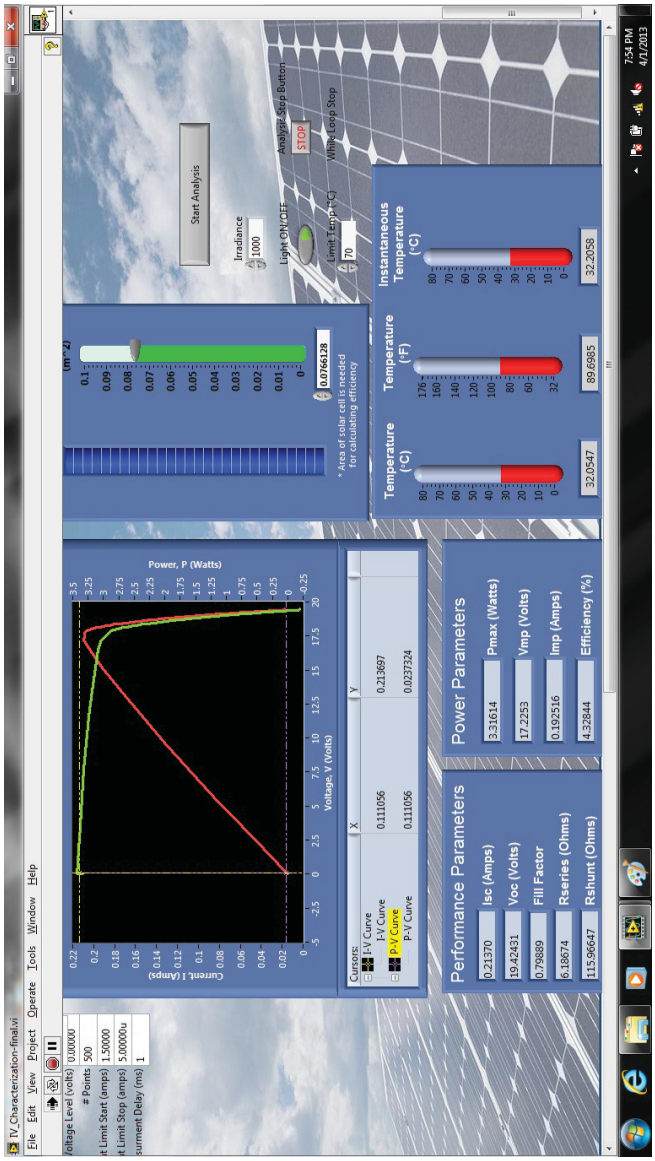

Figure A.5: Bare Panel at Steady State, $I = 1000\frac{W}{m^2}, V = 2.54\frac{m}{s}$

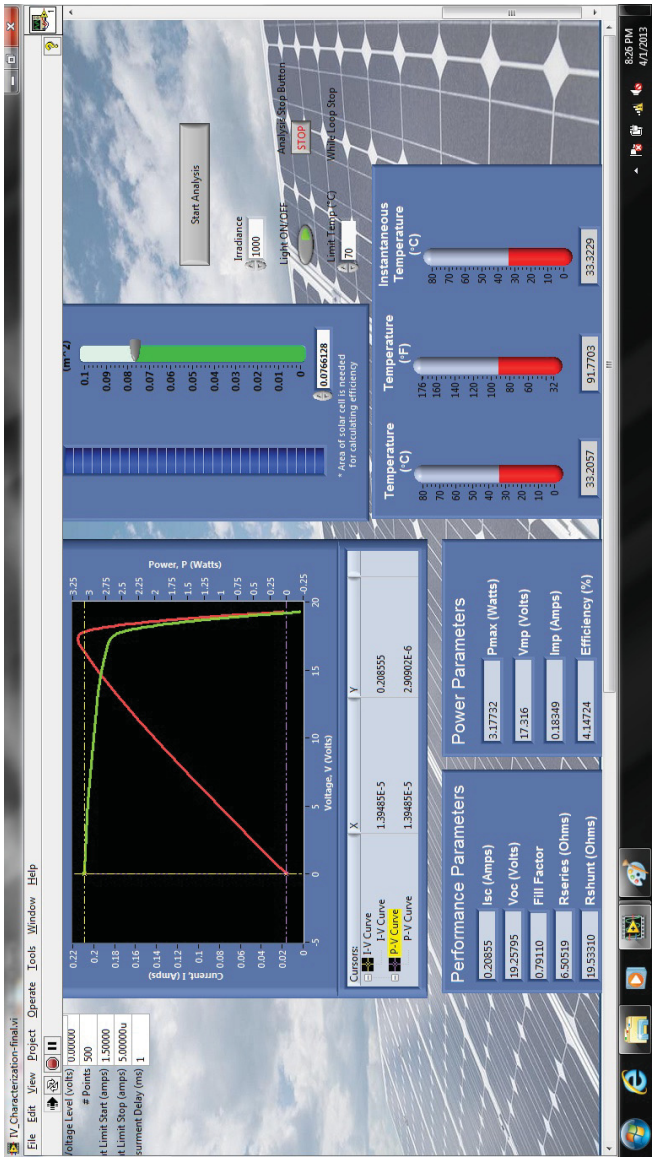

Figure A.6: Bare Panel at Steady State, $I = 1000\frac{W}{m^2}, V = 1.37\frac{m}{s}$

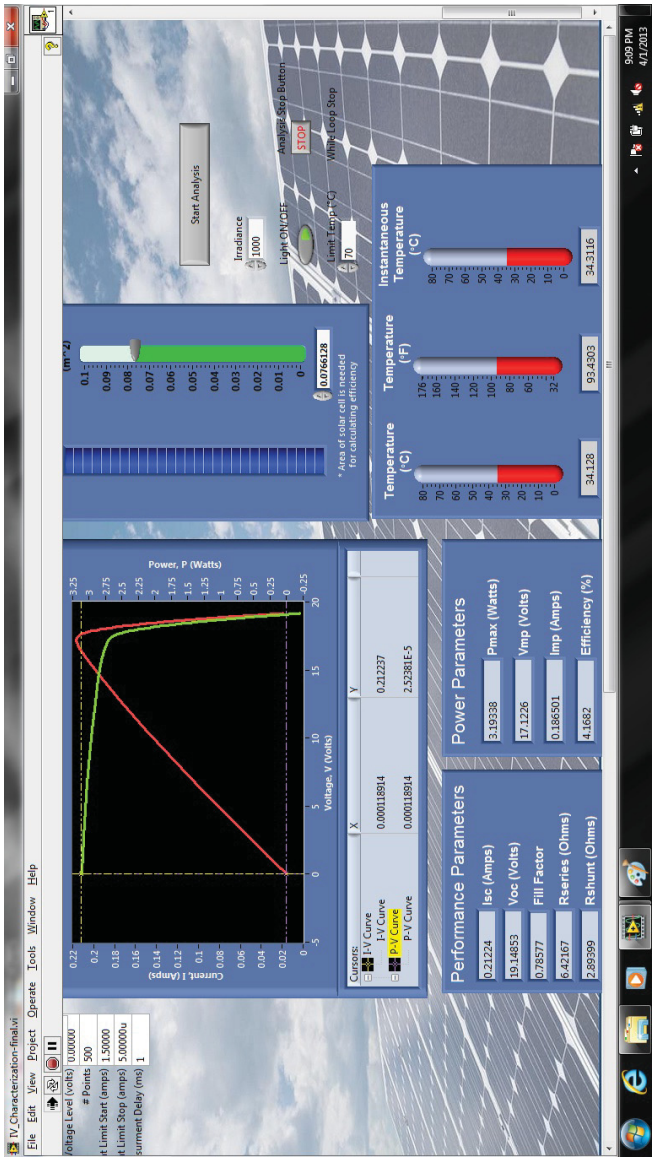

Figure A.7: Bare Panel at Steady State, $I = 1000\frac{W}{m^2}, V = 1.12\frac{m}{s}$

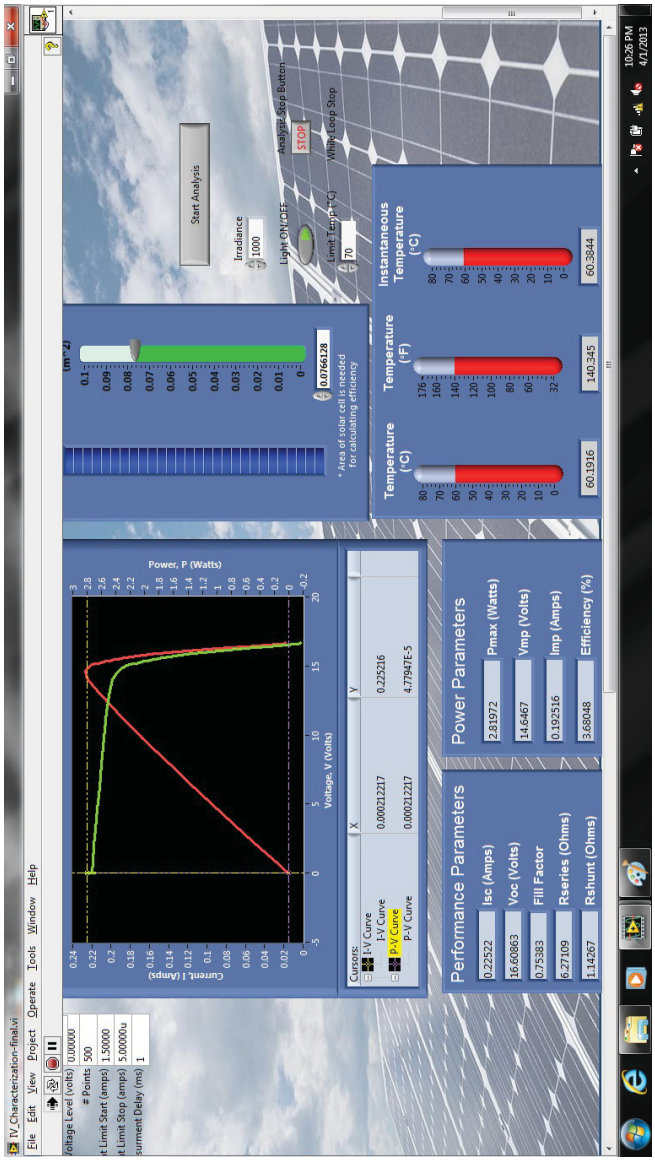

Figure A.8: Bare Panel at Steady State, $I = 1000\frac{W}{m^2}, V = 0\frac{m}{s}$